



# Orientational polarizability of solids induced by the Jahn-Teller and pseudo-Jahn-Teller effects

Victor Polinger <sup>1,\*</sup> and Isaac B. Bersuker <sup>2</sup>

<sup>1</sup>Department of Chemistry, *University of Washington*, 109 Bagley Hall, Seattle, Washington 98195, USA

<sup>2</sup>Oden Institute for Computational Engineering and Science, *The University of Texas at Austin*, Austin, Texas 78712, USA



(Received 6 February 2024; revised 2 May 2024; accepted 21 May 2024; published 24 June 2024)

We show that, in solids with Jahn-Teller effect (JTE) or pseudo-JTE (PJTE) centers, local dipolar displacements may occur, which are almost freely rotating in external electric fields (like in polar liquids), thus realizing solid-state orientational polarizability predicted by Debye [Phys. Z. **13**, 97 (1912)]. As illustrative examples, we consider impurity ions in noncentrosymmetric cubic crystals with a degenerate ground state coupled to polar modes of nearest neighboring ligands via the JTE and local centers in centrosymmetric crystals with electronic pseudodegeneracy realizing the PJTE. In the JTE  $T \otimes t_2$  problem in a tetrahedral site, the vibronic coupling to trigonal modes creates off-center shifted dipolar distortions of the dopant along one of the four equivalent minima of the adiabatic potential energy surface. Resonating between these wells by tunneling or over-the-barrier transitions, the dipoles perform hindered rotations in space, like molecular dipoles in polar liquids and gases. In external electric fields, the local dipolar minima become nonequivalent with the dipolar distortion trapped in the specific well, which is lowered by the applied field in the same direction in all the centers, thus realizing the solid-state orientational polarizability. Distinguished from the JTE case, the PJTE may produce off-center shifted dipolar distortions in both centrosymmetric and noncentrosymmetric sites, with the disordered local dipolar distortions resonating between the equivalent wells at each PJTE site. Under the applied electric field, the system becomes trapped in the lower well along the field. According to numeric estimates, the orientational contribution to polarizability is by orders of magnitude larger than the one from the displacive shifts of the charged units, quite similar to the orientational polarizability of polar liquids and gases.

DOI: [10.1103/PhysRevB.109.224207](https://doi.org/10.1103/PhysRevB.109.224207)

## I. INTRODUCTION

Debye [1] assumed that there may be solids containing rotating local dipoles (like in polar liquids), which may be subjects of orientational polarizability at temperatures above some freezing point. In such solids, the local induced polarization  $P$  in relatively weak electric fields is proportional to the average value  $\langle p \rangle$  of its electric dipole moment. Debye's estimate shows that this *orientational polarizability* may be larger than the electronic and nuclear displacive contributions by orders of magnitude.

Debye's [1] hypothetical assumption had no factual background then and did not find confirmation until the present works, yet it raised two questions: (a) Can local dipoles occur in centrosymmetric crystals, and (b) if there are such local dipole formations, are their bumpy (free or hindered) rotations possible in the solid crystal-field environment?

Although anomalously high polarizability  $\chi$  was soon found in some cubic perovskites (e.g., in  $\text{BaTiO}_3$ , at room temperature,  $\chi$  is of the order of 1200–10 000), its orientational nature was not understood until Bersuker [2] interpreted it as the characteristic feature of the local, freely rotating dipoles, produced by the vibronic coupling. For barium titanate, he deduced the off-center dipolar instability of the  $\text{Ti}^{4+}$  ions in  $\text{BaTiO}_3$  from the pseudo-Jahn-Teller effect (PJTE) [2].

The idea of spontaneous symmetry breaking in polyatomic systems emerged when Landau, in his discussion with

Teller [3], formulated the groundbreaking statement about the structural instability of symmetric molecules in the state of electronic degeneracy, presently known as the Jahn-Teller effect (JTE, see also Refs. [4–10]). In a cluster with the JTE, as described by Van Vleck [11], the adiabatic potential energy surface (APES) has a conical shape near the high-symmetry point of electronic degeneracy and a wrapped trough around it with a broken symmetry at each point. The energy gained from dropping to its bottom is called the Jahn-Teller (JT) stabilization energy  $E_{\text{JT}}$ . Small-radius nuclear motion along the JT trough is an ensemble movement of a relatively large number of atoms; they undergo a pseudorotation.

As it was soon realized, the exact electron degeneracy is not the only source of spontaneous symmetry breaking. A relatively small splitting  $\Delta$  of the degenerate term at the high-symmetry point [12] or any other two sufficiently close in energy electronic states of different origin [2] (electronic quasidegeneracy) may lead to the formation of lower-symmetry minima on the lowest branch of the APES, the phenomenon known today as the PJTE [2,7,8]. These discoveries underwent tremendous developments, also resulting in the so-called hidden JTE and PJTE [9]. Together, this series of JTEs destroyed the classical image of polyatomic formations with stable geometries, allowing for local dynamics along a wrapped trough on the APES shaped by the JTEs. Moreover, it opened options for explaining the structure and properties of polyatomic systems, including solids. Nuclear motion along the JTE or PJTE trough lies in the background of the orientational mechanism of polarizability, which was predicted by Debye more than a century ago.

\*vpolinger@msn.com

With the JTE- and PJTE-induced local dipolar instabilities, orientational polarizability in solids becomes a straightforward and physically transparent phenomenon. In the absence of external perturbations, the JTE-induced off-center displacements of a local center are of a dynamic nature. The tunneling or over-the-barrier transitions between equivalent minima are like rotations of dipoles in polar liquids. Under an applied electric field, the wells on the APES become nonequivalent, and the rotating dipole gets stuck in the lowest one. Hence, the local dipoles become field oriented in the same direction in all centers, thus realizing solid-state orientational polarizability, like polar liquids and gases.

In cubic crystal structures, local dipoles are due to off-center atomic displacements. Doping may result in JTE-induced local dipolar instability, significantly changing impurity-induced electric properties. Some dopants can be unstable to such displacements, even if the host crystal is stable to distortions. In noncentrosymmetric cubic crystals, the  $T_2$  mode includes local dipole-active nuclear displacements in the first coordination sphere. Indeed, according to the neutronography data, local polar distortions in a wide temperature range were observed in the doped crystal ZnO:Ni<sup>2+</sup> [13,14], which indicates a strong JTE in impurity tetrahedral sites [NiO<sub>4</sub>]. Most interesting is the drastic increase in permittivity of the ZnO crystal, >250 times, with just a 2% doping with Ni<sup>2+</sup> ions [15]. Early theoretical models and some experimental data are listed in Ref. [16].

In this paper, we give a complete theoretical description of the orientational contribution to permittivity due to the JTE and PJTE, which emerge as deviations from the Born-Oppenheimer approximation and are the cause of spontaneous symmetry breaking in polyatomic systems, including the local off-center instability in crystals under consideration [7,8]. In centrosymmetric crystals, off-center displacements are of odd symmetry, and they cannot be active in the JTE due to the parity selection rule. However, in the presence of two entangled states of opposite parity with a sufficiently small energy gap  $\Delta$ , odd-parity modes can be off-center unstable if the vibronic coupling in the corresponding PJTE meets the instability condition for these modes [2,7,12]. These can be ions with a closed-shell electron configuration like, for instance, the ground states of Li<sup>+</sup>, Na<sup>+</sup>, Mg<sup>2+</sup>, Al<sup>3+</sup>, or Ti<sup>4+</sup> in cubic sites of the crystal lattices with the structure of alkali halide, fluorite, or perovskite crystals.

On the other hand, in noncentrosymmetric crystals, the parity restriction does not apply, and the off-center instability can be due to a JTE for degenerate ground states. In tetrahedral symmetry, polar vector components transform as the irreducible representation  $T_2$ . As  $T_2$  modes are active in the JTE for an orbital triplet term, we consider dopants with the ground-state term  $T_1$  or  $T_2$ . Concerning the solids with JTE centers, the emphasis in this paper will be on tetrahedral dopant sites [NiS<sub>4</sub>]<sup>6-</sup> in ZnS: Ni<sup>2+</sup>, [NiSe<sub>4</sub>]<sup>6-</sup> in ZnSe: Ni<sup>2+</sup>, and [NiO<sub>4</sub>]<sup>6-</sup> in ZnO: Ni<sup>2+</sup>.

Sections II and III below introduce the basic concepts and formulas employed in the rest of this paper. Section II briefly describes separating the dopant off-center distortions and the so-called Born charge, which models their contribution to the polar displacements.

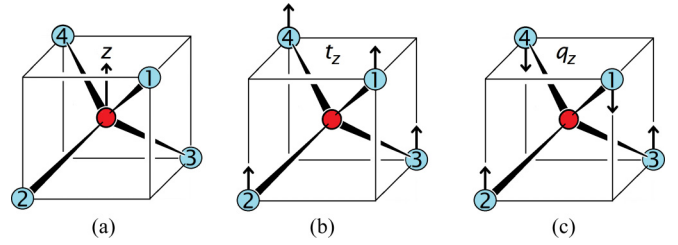


FIG. 1. The three sets of symmetry-adapted  $T_2$  type displacements  $\vec{r}$ ,  $\vec{t}$ , and  $\vec{q}$  in the tetrahedral cluster [MB<sub>4</sub>] with the dopant M (red circle) and ligand tetrahedron B<sub>4</sub> (blue circles). (a) The  $z$  component of the off-center displacement  $\vec{r}$  of the dopant M. (b) The  $z$  component of the rigid shift  $\vec{t}$  of the ligand tetrahedron B<sub>4</sub>. (c) The  $z$  component of the angle-bending mode  $\vec{q}$ .

Section III discusses the dynamics of the nuclei with the impurity ion tunneling between the equivalent wells of the APES. It includes the vibronic Hamiltonian in the so-called cluster model for a tetrahedron [MB<sub>4</sub>], octahedron [MB<sub>6</sub>], and cube [MB<sub>8</sub>] with the dopant ion M at its center and emphasizing the bonding nature of the JT type dipolar instability. To describe and evaluate the orientational polarizability, we apply the vibronic theory of dipolar instability [2], further developed for ferroelectric perovskites (see the latest in Ref. [17], sec. 6.2 in Ref. [7], and sec. 8.3 in Ref. [8]). The origin of the dipolar instability in the JTE is illustrated by the tetrahedral dopant site [MB<sub>4</sub>] and in the PJTE in the centrosymmetric octahedral and cubic sites [MB<sub>6</sub>] and [MB<sub>8</sub>].

Section IV presents our main results on orientational polarizability. It includes the JTE in temperature, angular, and field dependences of the electric susceptibility. We assume the JT coupling is sufficiently strong to justify the adiabatic approximation in the APES minima.

Section V illustrates the mechanism of orientational polarizability in cases when the local dipolar instability is due to the PJTE, notably in BaTiO<sub>3</sub>. Section VI applies the JTE- and PJTE-induced polarization to evaluate the corresponding orientational susceptibility of the high-symmetry tetrahedral, octahedral, and cubic sites. Finally, Secs. VII and VIII discuss the applicability of the results to specific systems and compare them with the experimental data.

## II. POLAR MODES IN TETRAHEDRAL, OCTAHEDRAL, AND CUBIC SITES

We begin with tetrahedral unit cells in cubic crystals. The binary semiconductors A<sup>II</sup>B<sup>VI</sup> and A<sup>III</sup>B<sup>V</sup>, with the sphalerite or wurtzite structure, such as ZnS or GaAs, may serve as typical examples of this kind. The dopant ion M substitutes the regular cation A, and it is tetrahedrally coordinated in both cases, surrounded by four anions (Fig. 1). We neglect the possible lower-symmetry crystal field corrections for simplicity, assuming tetrahedral symmetry  $T_d$  of the dopant site.

The problem is simplified significantly in the so-called cluster model. It reduces the consideration to just the dopant and its nearest neighbors. In the case of tetrahedral sites, the corresponding cluster is a five-atom molecule [MB<sub>4</sub>] with the

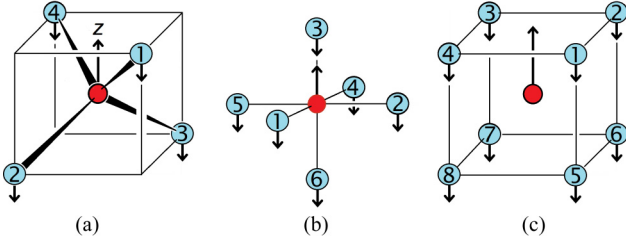


FIG. 2. The  $z$  component of the dipolar displacement  $\vec{R} = \vec{r} - \vec{i}$  of the central atom M (red circle) relative to nearest-neighbor ligands (shown in blue) in (a) tetrahedron  $[\text{MB}_4]$ , (b) octahedron  $[\text{MB}_6]$ , and (c) eight-coordinated cube  $[\text{MB}_8]$ .

metal M at its center and four ligands B at the vertices of the regular tetrahedron. Justification for the cluster model is at the end of Sec. III A.

For the regular tetrahedron  $[\text{MB}_4]$ , the components of a polar vector form the basis of the irreducible representation  $T_2$ . The five-atom tetrahedral molecule  $[\text{MB}_4]$  has three linearly independent symmetry-adapted sets of  $T_2$  modes. Figure 1 shows the  $z$  component of each of the three sets,  $\vec{r}$ ,  $\vec{i}$ , and  $\vec{q}$  [18]. Missing components  $x$  and  $y$  can be obtained by symmetry transformations of the group  $T_d$  applied to the displayed  $z$  component. The vector  $\vec{r} = (x, y, z)$  stands for off-center Cartesian displacements of the central atom M [Fig. 1(a)]. The set  $\vec{i} = \frac{1}{2}(\vec{r}_1 + \vec{r}_2 + \vec{r}_3 + \vec{r}_4)$  represents the rigid shift of the ligand tetrahedron  $B_4$  [Fig. 1(b)]. It is composed of the displacements of the four ligands  $\vec{r}_k$  with  $k = 1, 2, 3,$  and  $4$ , numbered as in Fig. 1(a). The third set  $\vec{q} = \frac{1}{2}(\vec{r}_2 + \vec{r}_3 - \vec{r}_1 - \vec{r}_4)$  includes angle-bending ligand displacements [Fig. 1(c)].

Rigid shifts of the entire tetrahedron  $[\text{MB}_4]$  do not change the bond lengths and angles of the cluster. Consequently, we neglect the vibronic coupling to this mode and assume the center of mass of the tetrahedron  $[\text{MB}_4]$  at rest,  $(4m\vec{i} + M\vec{r})/(4m + M) = 0$ , where  $M$  is the mass of the central atom M and  $m$  is the mass of the ligand B. The angle-bending displacement  $\vec{q}$  [Fig. 1(c)], being orthogonal to  $\vec{r}$  and  $\vec{i}$ , keeps the center of mass of the tetrahedron  $B_4$  at rest. Also, we set  $\vec{q} = 0$ , as it is not essential to forming the dipole moment of the cluster  $AB_4$ . Then  $\vec{i} = -M\vec{r}/(4m)$ . Relative to the rigid tetrahedron  $B_4$ , the off-center dipolar mode is  $\vec{R} = \vec{r} - \vec{i}$  [Fig. 2(a)]. Its effective mass is  $m^* = 4mM/(4m + M)$ . In the case of  $[\text{NiO}_4]$ , where  $M = 58$  u and  $m = 16$  u, we get  $\vec{i} = -M\vec{r}/(4m) \approx -0.91\vec{r}$ , while the effective mass is  $m^* \approx 30$  u. Similarly, for  $[\text{NiS}_4]$  with  $m = 32$  u, we come to  $\vec{i} \approx -0.45\vec{r}$  and  $m^* \approx 40$  u. For  $[\text{NiSe}_4]$  with  $m = 80$ , we find  $\vec{i} \approx -0.18\vec{r}$  and  $m^* \approx 49$  u, and for  $[\text{NiTe}_4]$  with  $m = 130$ , we get  $\vec{i} \approx -0.11\vec{r}$  and  $m^* \approx 52$  u.

In centrosymmetric cubic sites  $[\text{MB}_6]$  and  $[\text{MB}_8]$  with symmetry  $O_h$ , the parity of polar vectors is odd. Their com-

ponents form the basis of the irreducible representation  $T_{1u}$ . Like the tetrahedral case, both the octahedral site  $[\text{MB}_6]$  and the cubic site  $[\text{MB}_8]$  include three linearly independent symmetry-adapted sets of  $T_{1u}$  modes,  $\vec{r}$ ,  $\vec{i}$ , and  $\vec{q}$ . The physical meaning of the latter is like the one discussed above. Neglecting rigid shifts of  $[\text{MB}_6]$  and assuming that its center of mass remains at rest at the origin, we get:  $(6m\vec{i} + M\vec{r})/(6m + M) = 0$ . Also, as above, we set  $\vec{q} = 0$ . Then the off-center dipolar mode is  $\vec{R} = \vec{r} - \vec{i}$  [Fig. 2(b)], and therefore,  $\vec{i} = -M\vec{r}/(6m)$ . Similarly, for cubic clusters  $[\text{AB}_8]$  with eight anions B, the dipolar mode is  $\vec{R} = \vec{r} - \vec{i}$  [Fig. 2(c)], and we find  $\vec{i} = -M\vec{r}/(8m)$ .

Induced by an alternating electric field  $\vec{E}(\nu)$  of frequency  $\nu$ , the electric dipole moment  $\vec{p}(\nu)$  of the clusters  $[\text{MB}_4]$ ,  $[\text{MB}_6]$ , or  $[\text{MB}_8]$  includes both nuclear and electronic contributions  $\vec{p}(\nu) = \vec{p}_n(\nu) + \vec{p}_{el}(\nu)$ . In a high-frequency electromagnetic wave, due to inertia, the nuclear contribution is relatively small, and therefore,  $p_n(\nu) \ll p_{el}(\nu)$ . In a static external field, when  $\nu = 0$ , the nuclear contribution dominates  $p_n(0) > p_{el}(0)$ . For example, in  $\text{ZnO:Ni}^{2+}$  at 2% doping, the ratio  $p(\infty)/p(0) < 0.004$  [15]. In what follows, we consider constant electric fields with  $\nu = 0$  involving just the nuclear contribution  $\vec{p} \approx \vec{p}_n$ . Also, assuming low dopant concentrations, we neglect cooperative phenomena in the impurity subsystem.

To quantify the nuclear dipole moment  $\vec{p}_n$ , we express the dipolar shift of a positive dopant relative to negative ligands in terms of the Cartesian coordinates of each atom. In the tetrahedral case of  $[\text{MB}_4]$ , we have  $\vec{R} = \vec{r} - \vec{i} = \vec{r} - M\vec{r}/(4m) = [(4m + M)/(4m)]\vec{r}$ . For example, in the host crystals  $\text{ZnO}$ ,  $\text{ZnS}$ ,  $\text{ZnSe}$ , or  $\text{ZnTe}$ , the oxidation state of Zn is +2. In a rough estimate, its electric charge, reduced by covalency, is somewhat less,  $\sim 1.5e$ . Accordingly, in diatomic host crystals like  $\text{ZnO}$  or  $\text{ZnS}$ , the electric charge of each anion is close to  $-1.5e$ . Consequently, the electric charge of the tetrahedron  $B_4$  is  $4(-1.5e) = -6e$ . Then  $\vec{p}_n \approx e(1.5\vec{r} - 6\vec{i})$ . Plugging in  $\vec{i} = -M\vec{r}/(4m)$ , we come to  $\vec{p}_n \approx [1.5(m + M)/m]e\vec{r}$ . For example, in the case of  $[\text{NiO}_4]$  with  $M = 58$  u and  $m = 16$  u, we find  $\vec{p}_n \approx 7e\vec{r}$ . To simplify, we assign the effective charge to the dopant, the so-called Born charge  $Z_B e$  [19], with  $Z_B \approx 1.5(m + M)/m$ . This assumption reduces the polarization of the entire cluster to the off-center shift of the dopant  $\vec{r}$ . Then the induced dipole moment of the cluster is  $\vec{p} \approx \vec{p}_n = eZ_B\vec{r}$ . For  $[\text{NiO}_4]$ ,  $[\text{NiS}_4]$ ,  $[\text{NiSe}_4]$ , and  $[\text{NiTe}_4]$ , the corresponding values of  $Z_B$  are  $\sim 7, 4, 3,$  and  $2$ , respectively.

The off-center displacement of the central atom relative to the rigid octahedron  $B_6$  is  $\vec{R} = \vec{r} - \vec{i} = [(6m + M)/(6m)]\vec{r}$ . For  $[\text{LiCl}_6]$  with  $M = 7$  u and  $m = 35$  u, we find  $\vec{i} \approx -0.03\vec{r}$ . Similarly, for  $[\text{TiO}_6]$  with  $M = 48$  u and  $m = 16$  u, we get  $\vec{i} = -0.5\vec{r}$ . For  $[\text{LiO}_6]$  with  $M = 7$  and  $m = 16$ , we get  $\vec{i} \approx -0.07\vec{r}$ , and for  $[\text{NbO}_6]$  with  $M = 93$  and  $m = 16$ ,  $\vec{i} \approx -0.97\vec{r}$ . Similarly, in the case of a cubic site  $[\text{MB}_8]$ , we get

TABLE I. Rough estimates of Born charges  $Z_B$  (in units of  $e$ ) for some octahedral and cubic clusters  $[\text{MB}_6]$  and  $[\text{MB}_8]$ .

Crystal	KCl:Li <sup>+</sup>	KCl:Cu <sup>2+</sup>	KTaO <sub>3</sub> :Li <sup>+</sup>	KTaO <sub>3</sub> :Nb <sup>5+</sup>	KNbO <sub>3</sub>	BaTiO <sub>3</sub>	RbCl:Ag <sup>2+</sup>
Cluster	[LiCl <sub>6</sub> ]	[CuCl <sub>6</sub> ]	[LiO <sub>6</sub> ]	[NbO <sub>6</sub> ]	[NbO <sub>6</sub> ]	[TiO <sub>6</sub> ]	[AgCl <sub>8</sub> ]
$Z_B$	1	2	2	9	9	7	2

TABLE II. Examples of  $3d$  impurity ions with an orbital triplet  $^{2S+1}T$  ground state in tetrahedral sites  $[\text{MB}_4]$  (see Ref. [20]).

$d^n$	Dopant	High spin (weak-field ligands, small $e-t_2$ -splitting)		Low spin (strong-field ligands, large $e-t_2$ -splitting)	
		Configuration	Ground state	Configuration	Ground state
$d^3$	$\text{V}^{2+}, \text{Cr}^{3+}$	$(e^* \uparrow)^2 (t_2^* \uparrow)^1$	${}^4T_1$		
$d^4$	$\text{Cr}^{2+}, \text{Mn}^{3+}$	$(e^* \uparrow)^2 (t_2^* \uparrow)^2$	${}^5T_2$		
$d^5$	$\text{Mn}^{2+}, \text{Fe}^{3+}$			$(e^* \uparrow)^2 (e^* \downarrow)^2 (t_2^* \uparrow)^1$	${}^2T_2$
$d^6$	$\text{Fe}^{2+}, \text{Co}^{3+}$			$(e^* \uparrow)^2 (e^* \downarrow)^2 (t_2^* \uparrow)^2$	${}^3T_1$
$d^8$	$\text{Ni}^{2+}$	$(e^* \uparrow)^2 (e^* \downarrow)^2 (t_2^* \uparrow)^3 (t_2^* \downarrow)^1$	${}^3T_1$		${}^3T_1$ [21]
$d^9$	$\text{Cu}^{2+}$	$(e^* \uparrow)^2 (e^* \downarrow)^2 (t_2^* \uparrow)^3 (t_2^* \downarrow)^2$	${}^2T_2$	$(e^* \downarrow)^2 (t_2^* \uparrow)^3 (t_2^* \downarrow)^2$	${}^2T_2$ [21]

$\vec{r} = [(8m + M)/(8m)]\vec{r}$ . Table I shows the rough estimates of Born charges for some octahedral and cubic clusters.

### III. JTE AND PJTE IN TETRAHEDRAL AND CUBIC CENTERS

In the tetrahedral site  $[\text{MB}_4]$  with the symmetry  $T_d$ , components of polar vectors form the basis of the irreducible representation  $T_2$ ; hence, the dipolar  $T_2$  modes contribute to its dipole moment. Therefore, following the JT theorem [4], tetrahedral and cubic polyatomic systems in the electron threefold degenerate state  $T_1$  or  $T_2$  may be unstable about the trigonal  $t_2$  polar distortions. As the triplet terms are coupled to both tetragonal and trigonal vibrations  $e$  and  $t_2$ , this brings us to the  $T \otimes (e + t_2)$  JTE problem [7,8], yielding an APES with trigonal wells when vibronic coupling to the  $t_2$  modes dominates [12]. To simplify further consideration, we assume that the vibronic coupling to the tetragonal  $e$  modes is negligibly weak, reducing the JT problem to  $T \otimes t_2$ .

The electron triplet ground states  $T_1$  and  $T_2$  are due to the electron population of a specific sequence of the lowest-energy one-electron molecular orbitals (MOs) [20]. For a transition-metal  $3d^n$  ion M in  $[\text{MB}_4]$ , the tetrahedral crystal field splits the five atomic orbitals  $3d$  into a low-energy twofold degenerate orbital  $e(3d)$  and a higher-energy threefold orbital  $t_2(3d)$  (in octahedral and cubic fields, this splitting is inverse). The resultant sequence of MOs is determined by the covalent chemical bonding of the central atom M with the four ligands B [20]; the open-shell five valence  $3d$  orbitals form antibonding MOs with lower-energy orbital  $e^*$  and higher-energy orbital  $t_2^*$ . Following the Pauli principle, the electrons occupy the lowest-energy MOs in opposite-spin pairs on each of them in the ground state. Subject to the relative strength of the interatomic repulsion vs the crystal field, this electron population scheme results in either a low- or a high-spin electron configuration. The two options depend on the crystal-field strength of the ligand, the  $e - t_2$ -splitting, or in other words, on the position of ligand B in the spectrochemical series [20]. Table II shows examples of transition-metal dopants in  $[\text{MB}_4]$  sites in tetrahedral  $T_d$  symmetry with the ground-state  $^{2S+1}T$  term [20] (with the same dopant M, high-spin, and low-spin cases representing different B ligands).

In addition to the vibronic coupling, in all these cases, the effects of spin-orbital interaction play an essential role in reducing the JTE. This paper focuses on the orientational polarization in solids induced by vibronic effects (the JTE and PJTE), the implication of spin-orbital coupling being left for a later publication.

Compared with the interatomic distances in the impurity cluster, polar displacements of its atoms are relatively small. We expand the Hamiltonian of the impurity site in terms of the off-center displacements of the central ion M. The JTE Hamiltonian for a  $T_1$  or  $T_2$  state takes the standard form  $H = H_0 + H_{\text{ph}} + H_{\text{JT}}$ . For certainty, in what follows, we assume the electron term to be  $T_1$ ; in the case of a  $T_2$  term, all the formulas and the corresponding conclusions remain the same. Here,  $H_0$  is the electron Hamiltonian,  $H_0 = E_0[|\alpha\rangle\langle\alpha| + |\beta\rangle\langle\beta| + |\gamma\rangle\langle\gamma|]$ . It represents the degenerate  $T_1$  term with the reference energy  $E_0$  of the three degenerate orbital states  $|\alpha\rangle$ ,  $|\beta\rangle$ , and  $|\gamma\rangle$ ; indices  $\alpha$ ,  $\beta$ , and  $\gamma$  label rows of the irreducible representation  $T_1$ . Here and in what follows below, to distinguish the ground-state vibronic wave functions  $|\alpha\rangle$ ,  $|\beta\rangle$ , and  $|\gamma\rangle$  from the orbital states  $|\alpha\rangle$ ,  $|\beta\rangle$ , and  $|\gamma\rangle$  of the electron  $T_1$  term with the same transformation properties, we use angular brackets for the former and parentheses for the latter. In the case of the JTE, the electron Hamiltonian  $H_0$  is proportional to the unit matrix  $|\alpha\rangle\langle\alpha| + |\beta\rangle\langle\beta| + |\gamma\rangle\langle\gamma|$ , an invariant of any unitary transformations. Selecting the reference energy  $E_0 = 0$  eliminates  $H_0$  from further consideration. On the other hand, in the case of a PJTE, considered in Sec. III B below, the Hamiltonian  $H_0$  includes the energy gap between the participating electron terms. It is not proportional to the unit matrix, and setting  $E_0 = 0$  does not eliminate  $H_0$ .

Here,  $H_{\text{ph}} = T_{\text{ph}} + U_{\text{ph}}$  is the phonon Hamiltonian of the crystal lattice,  $T_{\text{ph}}$  is the kinetic energy, and  $U_{\text{ph}}$  is the harmonic potential energy of the nuclei. Applying the cluster model (its justification is at the end of Sec. III C) reduces the phonon degrees of freedom to the nine vibrations of the tetrahedron  $[\text{MB}_4]$ . As discussed in Sec. II, by introducing the Born charge, we reduce the dipolar modes to the off-center shift of the central atom  $\vec{r} = (x, y, z)$ . In this approximation,

$$T_{\text{ph}} = \frac{1}{2}(p_x^2 + p_y^2 + p_z^2), \quad U_{\text{ph}} = \frac{1}{2}\omega_0^2(x^2 + y^2 + z^2), \quad (1)$$

where  $p_x$ ,  $p_y$ , and  $p_z$  are linear momenta conjugated to the mass-weighted coordinates  $x$ ,  $y$ , and  $z$ , respectively, and  $\omega_0$  is the reference (bare) frequency of the dipolar mode.

Assuming that the radius of the impurity center is sufficiently small, we add the linear electron-vibrational (vibronic) coupling interactions to just the off-center Cartesian displacements of the dopant  $x$ ,  $y$ , and  $z$ . Hence,  $H_{\text{JT}} = V(x\mathbf{C}_x + y\mathbf{C}_y + z\mathbf{C}_z)$  is the Hamiltonian of linear JT (vibronic) coupling at the impurity site [7,8]. The  $3 \times 3$  matrices:

$$\begin{aligned} \mathbf{C}_x &= -|\beta\rangle\langle\gamma| - |\gamma\rangle\langle\beta|, \\ \mathbf{C}_y &= -|\alpha\rangle\langle\gamma| - |\gamma\rangle\langle\alpha|, \\ \mathbf{C}_z &= -|\alpha\rangle\langle\beta| - |\beta\rangle\langle\alpha|, \end{aligned} \quad (2)$$

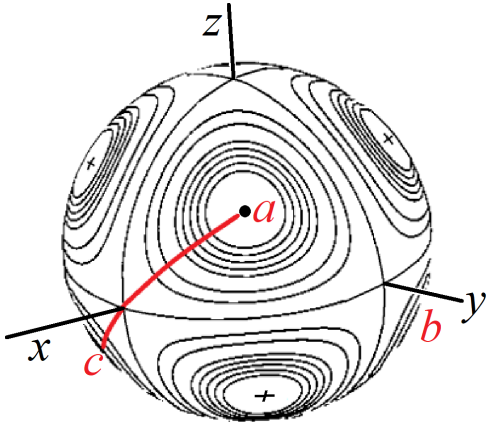


FIG. 3. Equipotential cross-sections of the lower-sheet adiabatic potential energy surface (APES)  $U_0(x, y, z)$ . Bold dots (just one is seen) denote the symmetry directions  $[111]$  (direction of the trigonal minimum  $a$ ),  $[\bar{1}\bar{1}\bar{1}]$  (direction of the minimum  $b$ ), etc. Circles with the dots indicate trigonal wells. The minimum  $d$  is on the back side of this sphere and is not seen. The crosses indicate saddle points. The red curve  $ac$  shows the paths of steepest descent from the orthorhombic saddle point on the symmetry axis  $[100]$  to the minimum points  $a$  and  $c$ .

represent electron operators  $(\partial H/\partial x)_0$ ,  $(\partial H/\partial y)_0$ , and  $(\partial H/\partial z)_0$  in the symmetry-adapted basis set of the three degenerate orbital states  $|\alpha\rangle$ ,  $|\beta\rangle$ , and  $|\gamma\rangle$ . The index 0 indicates the regular tetrahedron  $[\text{MB}_4]$ . According to the Wigner-Eckart theorem, for matrices  $\mathbf{C}_x$ ,  $\mathbf{C}_y$ , and  $\mathbf{C}_z$ , matrix elements are the corresponding Clebsch-Gordan coefficients. The common factor  $V$  is the reduced matrix element of these operators, the so-called vibronic coupling constant. It incorporates the common factor  $1/\sqrt{2}$  of each Clebsch-Gordan coefficient. Since  $H_{\text{JT}}$  includes electron matrices  $\mathbf{C}_x$ ,  $\mathbf{C}_y$ , and  $\mathbf{C}_z$ , it is also a  $3 \times 3$  matrix operating in the basis space of three orbital states  $|\alpha\rangle$ ,  $|\beta\rangle$ , and  $|\gamma\rangle$ .

Still, after all the approximations have been applied, the vibronic Hamiltonian  $H = H_0 + H_{\text{ph}} + H_{\text{JT}}$  is too complex. The next step is the adiabatic separation of nuclear motion. For applicability, the energy gap between the ground-state electron term and the upper one has to be large enough compared with the local vibrations frequency  $\hbar\omega_0$ . Due to the JTE, the high-symmetry configuration is unstable. However, in most cases, the vibronic coupling is sufficiently strong, and the degenerate  $T_1$  term splitting is sufficiently large to allow the adiabatic approximation.

#### A. JTE-induced APES in systems with an electronic $T_1$ term

In the adiabatic approximation, at its first step, we neglect the kinetic energy  $T_{\text{ph}}$  of the nuclei. Then the Hamiltonian  $H = T_{\text{ph}} + U_{\text{ph}} + H_{\text{JT}}$  simplifies to just the potential energy matrix  $\mathbf{U}_{\text{JT}} = U_{\text{ph}} + H_{\text{JT}}$ , with  $U_{\text{ph}}$  from Eq. (1), and  $H_{\text{JT}} = V(x\mathbf{C}_x + y\mathbf{C}_y + z\mathbf{C}_z)$ . Eigenvalues of this  $3 \times 3$  matrix are the APESs for nuclei [7,8]. The vibronic coupling term dominates at the small vicinity of the high-symmetry on-center position of the dopant, creating a conic intersection of the APES with the off-center JTE instability of the dopant at  $\vec{r} = 0$ . At larger values

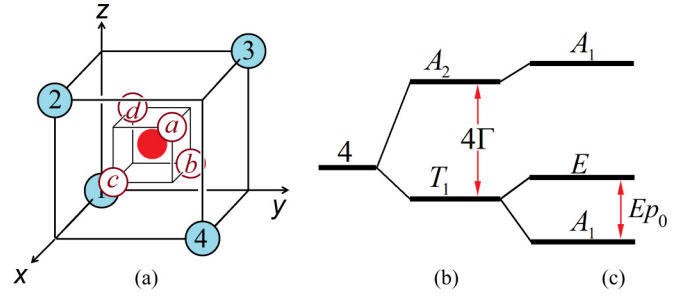


FIG. 4. Strong off-center instability in tetrahedral sites  $[\text{MB}_4]$  due to the Jahn-Teller effect (JTE)  $T_1 \otimes t_2$  problem and the corresponding ground-state energy-level diagram. (a) Four off-center equilibrium adiabatic potential energy surface (APES) minima positions (white circles labeled  $a$ ,  $b$ ,  $c$ , and  $d$ ) of the dopant M (red circle). (b) Tunneling lifts this degeneracy resulting in the ground-state tunneling triplet term  $T_1$  and excited tunneling singlet  $A_2$ . The corresponding energy gap between them is  $4\Gamma$  (Sec. III C). (c) Stark-effect splitting (not to scale) of the ground-state tunneling  $T_1$  term.

of  $x$ ,  $y$ , and  $z$ , combined with the elastic energy of nuclei  $U_{\text{ph}}$ , the vibronic coupling term determines low-symmetry wells on the lower branch of the APES  $U_0(\vec{r})$ .

According to Öpik and Pryce [12] (see also Refs. [7,8]), in this case, there are four symmetry-equivalent trigonal wells:  $a$ ,  $b$ ,  $c$ , and  $d$  on the lowest branch of the APES. Instead of the high-symmetry on-center position at  $\vec{r} = 0$ , stable positions (minima of the APES) of the JTE dopant are at the low-symmetry off-center trigonal points (Fig. 3):

$$\begin{aligned}\vec{r}_a &= r_0(1, 1, 1), \\ \vec{r}_b &= r_0(1, -1, -1), \\ \vec{r}_c &= r_0(-1, 1, -1), \\ \vec{r}_d &= r_0(-1, -1, 1),\end{aligned}\quad (3)$$

with  $r_0 = 2V/(3\omega_0^2)$  [12]. In each of the trigonal wells, the off-center shift of the dopant is  $R_0 = \sqrt{x^2 + y^2 + z^2} = r_0\sqrt{3}$ , and the overall symmetry of the cluster reduces to trigonal  $T_d \rightarrow C_{3v}$  [Fig. 4(a)]. The electron  $T_1$  term splits into the ground-state trigonal singlet and the excited-state doublet  $T_1 \rightarrow A_2 + E$ . The corresponding ground-state potential energy is  $U_0(C_{3v}) = U_0(\vec{r}_a) = U_0(\vec{r}_b) = U_0(\vec{r}_c) = U_0(\vec{r}_d) = -E_{\text{JT}}$ , which is the so-called JTE stabilization energy  $E_{\text{JT}} = 2V^2/(3\omega_0^2)$  [12]. At each point with the coordinates in Eq. (3), the trigonal  $E$  term is above the trigonal singlet by the energy gap of  $3E_{\text{JT}}$  [12].

The saddle points at the top of the APES barriers separate trigonal wells. One of them is at  $\vec{r} = 1.5r_0(0, 0, 1)$ , corresponding to the off-center shift of the central atom in one of the six symmetry-equivalent directions of the improper-rotational fourth-order axes. By reducing the tetrahedral symmetry to pyramidal  $T_d \rightarrow C_{2v}$ , this distortion drops the potential energy down to the value of  $U_0(C_{2v}) = -\frac{3}{4}E_{\text{JT}}$  [12]. The red curve on the sphere of Fig. 3 is the path of steepest descent from this saddle point to the trigonal wells  $a$  and  $d$ . The height of the corresponding potential barriers is  $\Delta U_0 = U_0(C_{2v}) - U_0(C_{3v}) = -\frac{3}{4}E_{\text{JT}} - E_{\text{JT}} = \frac{1}{4}E_{\text{JT}}$ .

Due to the JTE for the  $T$  term, either  $T_1 \otimes t_2$  or  $T_2 \otimes t_2$ , the ground-state branch  $U_0(\vec{r})$  of the APES is a wrapped two-dimensional trough. Generally, the size of potential barriers on its bottom depends on the vibronic coupling to the tetragonal  $E$  modes and the higher-order terms of vibronic interaction. In addition to the abovementioned extremes, the APES has other stationary points. For illustration, Fig. 3 qualitatively conveys the landscape of  $U_0(\vec{r})$  by its equipotential cross-sections with the sphere  $x^2 + y^2 + z^2 = r^2$ .

The above results are accurate to the extent they follow the symmetry of the dopant site. For example, all the extremes are on the symmetry axes of the tetrahedron, an exact outcome that does not depend on the accepted approximations [22–25]. They are due to the symmetry invariance of the lower branch APES in the subspace of the off-center coordinates  $\vec{r} = \langle x, y, z \rangle$ . In this respect, the landscape of the APES is similar in all cases of the JTE and PJTE involving the  $T_2$  mode. The wrapped two-dimensional trough is a general feature for all these cases. In what follows, the low-energy part of the energy-level diagram is most important for the effects of orientational polarizability. Note, however, that the vibronic coupling constants and the frequencies of dipole oscillations are approximate. Accordingly, the magnitude of the off-center shift  $R_0$  and the JTE stabilizing energy  $E_{JT}$  are subject to the adopted model.

Assume that the system is constrained to angular motion on the sphere  $x^2 + y^2 + z^2 = r^2$ . On the trough, where  $x = R_0 \sin\theta \cos\varphi$ ,  $y = R_0 \sin\theta \sin\varphi$ , and  $z = R_0 \cos\theta$ , it moves along the angles  $\theta$  and  $\varphi$ . The so-called Devonshire model yields an approximate expression for the bottom of the lower branch of the APES  $U_0(\vec{r})$  [26], which in its extended version is as follows [27]:

$$W(\theta, \varphi) \approx kE_{JT}[V_4(\theta, \varphi) \cos \mu + V_6(\theta, \varphi) \sin \mu]. \quad (4)$$

The two terms:

$$V_4(\theta, \varphi) = Y_4^0(\theta, \varphi) + \sqrt{\frac{5}{14}}[Y_4^4(\theta, \varphi) + Y_4^{-4}(\theta, \varphi)],$$

and

$$V_6(\theta, \varphi) = Y_6^0(\theta, \varphi) + \sqrt{\frac{21}{231}}[Y_6^6(\theta, \varphi) + Y_6^{-6}(\theta, \varphi)],$$

are low-order cubic harmonics. The two adjustment parameters  $k$  and  $\mu$  determine the strength of the potential and the relative contribution of  $V_4(\theta, \varphi)$  and  $V_6(\theta, \varphi)$ . Their numeric values result from  $U_0(\vec{r})$  at selected points, say, minima and saddle points, estimated in electronic structure calculations. At  $\mu = 0$ , we have the original Devonshire's model with just the fourth-order term,  $W(\theta, \varphi) = kE_{JT}V_4(\theta, \varphi)$  [26], coinciding with O'Brien's [28] approximate potential for the JTE in the linear  $T \otimes (e + t_2)$  case. When  $\mu \neq 0$ , the potential  $W(\theta, \varphi)$  includes the sixth-order term  $V_6(\theta, \varphi)$  providing energy adjustment for saddle points. At a positive value of  $k$ , the wrapped trough has six tetragonal wells. For  $k < 0$ , there are eight trigonal wells. By varying the parameter  $\mu \neq 0$ , we can have three different types of absolute minima. At  $k > 0$ , with  $\mu$  in the interval  $(-65^\circ, 26^\circ)$ , we get six tetragonal wells, with  $\mu$  in  $(26^\circ, 173^\circ)$ , there are 12 orthorhombic minima, and at

$\mu$  in the interval  $(173^\circ, 295^\circ)$ , the wrapped trough has eight trigonal wells [27].

## B. APES of nondegenerate electron terms shaped by a PJTE

Irrelevant to the JTE, spontaneous symmetry breaking may occur due to a PJTE, provided its vibronic entanglement with an excited state is strong enough [2,5–10,12]. As in Eqs. (1) and (2), the corresponding coupling constants are matrix elements of the operators of vibronic interaction  $(\partial H/\partial Q_{\Gamma\gamma})_0$ , mixing the electron ground state  $|\Gamma_1\gamma_1\rangle$  with an excited state  $|\Gamma_2\gamma_2\rangle$ . Here, the index 0 indicates the regular polyhedron [MB<sub>n</sub>];  $Q_{\Gamma\gamma}$  are symmetry-adapted normal modes of vibrations; index  $\Gamma\gamma$  specifies transformation properties of  $Q_{\Gamma\gamma}$  in the corresponding symmetry group;  $\Gamma$ ,  $\Gamma_1$ , and  $\Gamma_2$  stand for irreducible representations; and  $\gamma$ ,  $\gamma_1$ , and  $\gamma_2$  indicate their respective rows. Generally, the vibronic entanglement with the PJTE may include more electron terms than just two energy levels. Even in this two-level setup, the number of cases with the PJTE is significantly greater than the ones with the JTE.

Consider central-symmetric cubic sites with the point group  $O_h$ , like the six-coordinated [MB<sub>6</sub>] or eight-coordinated [MB<sub>8</sub>] clusters. For the dopant M, its off-center displacement  $\vec{r} = (x, y, z)$  transforms as  $\Gamma = T_{1u}$ . According to group-theoretical selection rules, within the basis set of degenerate states of the same electron ground term  $\Gamma_1$ , for the vibronic operators  $(\partial H/\partial x)_0$ ,  $(\partial H/\partial y)_0$ , and  $(\partial H/\partial z)_0$ , all their matrix elements  $(\Gamma_1\gamma_1|(\partial H/\partial r_i)_0|\Gamma_1\gamma_2)$  equal zero due to the parity restrictions. Therefore, no JTE is possible with the involvement of the dipolar coordinates  $T_{1u}$ . However, for electronic terms  $\Gamma_1$  and  $\Gamma_2$  of opposite parity, this restriction is lifted, and the matrix elements are not zero  $(\Gamma_1\gamma_1|(\partial H/\partial r_i)_0|\Gamma_2\gamma_2) \neq 0$ , provided the product  $\Gamma_1 \times \Gamma_2$  includes  $T_{1u}$ . Entangling electron states of opposite parity can contribute to vibronic symmetry breaking if the PJTE is strong enough [2,5–10,12].

For a cubic symmetry  $O_h$ , its ground electron term can be even  $\Gamma_1 = A_{1g}, A_{2g}, E_g, T_{1g}, T_{2g}$  or odd  $\Gamma_1 = A_{1u}, A_{2u}, E_u, T_{1u}, T_{2u}$ . In a two-level setup, under condition  $T_{1u} \in \Gamma_1 \times \Gamma_2$  with the PJTE-active  $T_{1u}$  mode, there can be several cases with an even ground state  $(A_{1g} + T_{1u}) \otimes t_{1u}$ ,  $(A_{2g} + T_{2u}) \otimes t_{1u}$ ,  $(E_g + T_{1u}) \otimes t_{1u}$ ,  $(E_g + T_{2u}) \otimes t_{1u}$ , etc., or an odd one  $(A_{1u} + T_{1g}) \otimes t_{1u}$ ,  $(A_{2u} + T_{2g}) \otimes t_{1u}$ ,  $(E_u + T_{1g}) \otimes t_{1u}$ ,  $(E_u + T_{2g}) \otimes t_{1u}$ , etc. In its turn, the first excited electron term  $T_{1u}$  may couple to other excited terms  $\Gamma_g$  of opposite parity via the dipolar modes  $T_{1u}$  whenever the group-theoretical selection rule for the corresponding matrix elements applies  $T_{1u} \times T_{1u} = \Gamma_g$ . All these arguments are relevant to the clusters with an orbital singlet ground state  $A_{2g}, A_{1u}$ , or  $A_{2u}$ . In all these cases, the vibronic Hamiltonian is similar, and at strong vibronic coupling, the lower-branch APES has the same landscape with similar wells and saddle points as in the JTE case.

In a three-level setup, more cases are possible  $(A_{1g} + A_{2g} + T_{1u}) \otimes t_{1u}$ ,  $(A_{1g} + T_{1u} + T_{2u}) \otimes t_{1u}$ , etc. In all these cases, extremes of the lower-branch APES are on cubic symmetry axes. This exact outcome does not depend on the accepted approximations. It is due to the symmetry invariance of the lower branch APES in the subspace of the off-center coordinates  $\vec{r} = (x, y, z)$  [22–25]. In this respect, qualitatively, the landscape of the APES is similar in all cases of the JTE and

TABLE III. Examples of  $M(3d^n)$  impurity ions with the ground state  $^{2S+1}A_1$  or  $^{2S+1}A_2$  in tetrahedral sites  $[MB_4]$  (see Ref. [20]).

$d^n$	Dopant	High spin (weak field, small $e-t_2$ -splitting)		Low spin (strong field, large $e-t_2$ -splitting)	
		Configuration	Ground state	Configuration	Ground state
$d^2$	$Ti^{2+}, V^{3+}$	$(e^* \uparrow)^2$	$^3A_2$		$^3A_2$ [21]
$d^4$	$Cr^{2+}, Mn^{3+}$			$(e^* \uparrow)^2(e^* \downarrow)^2$	$^1A_1$
$d^5$	$Mn^{2+}, Fe^{3+}$	$(e^* \uparrow)^2(t_2^* \uparrow)^3$	$^6A_1$		
$d^7$	$Co^{2+}, Ni^{3+}$	$(e^* \uparrow)^2(e^* \downarrow)^2(t_2^* \uparrow)^3$	$^4A_2$		$^4A_2$ [21]
$d^{10}$	$Cu^+, Zn^{2+}$			$(e^* \uparrow)^2(e^* \downarrow)^2(t_2^* \uparrow)^3(t_2^* \downarrow)^3$	$^1A_1$

PJTE involving the  $T_{1u}$  mode; it has the same minima and saddle points.

In what follows, we explore the tunneling model, describing the dopant dynamics by a single parameter  $\Gamma$ , the reciprocal probability of quantum tunneling through potential barriers between symmetry-equivalent wells on the lower branch of the APES. Therefore, it does not matter which PJTE case is under consideration. Here, the critical feature is the energy-level diagram of the ground-state tunneling multiplet, which depends on the characteristic features of the APES. Therefore, as an example, in what follows, we consider PJTE for just the two-level case with a ground-state orbital singlet  $(A_1 + T_2) \otimes t_2$  or  $(A_2 + T_1) \otimes t_2$  for a tetrahedral cluster  $[MB_4]$  and  $(A_{1g} + T_{1u}) \otimes t_{1u}$  or  $(A_{2g} + T_{2u}) \otimes t_{1u}$  for centrosymmetric clusters  $[MB_6]$ ,  $[MB_8]$ , or  $[MB_{12}]$ .

Assume that the ground state of the dopant is an orbital singlet  $^1A_1$ , like in the closed-shell low-spin case of  $Mn^{2+}$  in a tetrahedral site  $[MB_4]$  or  $Ti^{4+}$  in an octahedral site  $[MB_6]$ . The absolute minimum of the ground-state APES may be off-center shifted with  $\vec{r} \neq 0$  if the vibronic coupling to the  $T_{1u}$  mode is sufficiently strong [2,6], meaning the vibronic coupling constant  $F = \langle A_1 | (\partial H / \partial r_j)_0 | T_2 \gamma \rangle$  is strong enough. Table I lists several examples of off-center instability due to the PJTE. Table III shows examples of transition-metal dopants in tetrahedral sites  $[MB_4]$  with a singlet ground state  $^{2S+1}A_1$  or  $^{2S+1}A_2$ .

Table IV shows several examples of transition-metal dopants in octahedral and cubic sites  $[MB_6]$  or  $[MB_8]$  of  $O_h$  symmetry with a singlet ground-state  $^{2S+1}A_{1g}$  or  $^{2S+1}A_{2g}$  [20]. For cubic perovskites, the crucial role of the PJTE in the off-center symmetry breaking was revealed more than half a century ago [2]; it was further developed in recent years [16,17,29]. For example, the vibronic coupling of the ground state  $A_{1g}$  to the excited  $T_{1u}$  term determines the ferroelectric instability of  $Ti^{4+}$  in  $BaTiO_3$  [2,7].

The vibronic coupling creates a symmetry-destabilizing vibronic force with the force constant  $K_v = 4F^2/\Delta$ , where  $2\Delta$  is the energy gap separating the excited  $T_{1u}$  term from the ground state  $A_{1g}$ . The off-center instability occurs when the symmetry-destabilizing value  $K_v$  is larger than the symmetry-restoring reference elasticity  $K_v > K_0$  [2,7,8]. In this case, in the close vicinity of the high-symmetry point at  $\vec{r} = 0$ , the lowest branch of the APES has the shape of an open-down paraboloid. The coupling constant  $F$  reflects the rate of change of the covalence bonding induced by the off-center displacements. It leads to an enhancement of the chemical bonding of the ligands to the cation  $M$  with its off-center shift [7–9,30].

In the simplest case of a linear  $(A_{2g} + T_{1u}) \otimes t_2$  problem with a strong PJTE, a two-dimensional equipotential trough of minima occurs at the bottom of the potential  $U_0(\vec{r})$ . Generally, the PJTE may include more than just linear vibronic coupling and more than just one excited electron term  $T_{1u}$ . These effects add warping to the trough, producing minimum and saddle points on its bottom. As mentioned above, their symmetry transformation properties depend on the undistorted crystal structure, not the approximations employed in their treatment [22–25]. They are due to the symmetry invariance of the lower branch APES in the  $T_{1u}$  subspace of the off-center coordinates  $\vec{r} = (x, y, z)$ .

In what follows, we consider the case of strong vibronic coupling and low temperatures when the nuclear motion is localized at the bottom of the trough of the APES. Like the JTE in the tetrahedral site, introducing spherical coordinates  $x = R_0 \sin\theta \cos\varphi$ ,  $y = R_0 \sin\theta \sin\varphi$ , and  $z = R_0 \cos\theta$ , we assume that the dopant moves along  $\theta$  and  $\varphi$  directions. Then the same Devonshire model of Eq. (4) applies to the angular dependence of the lower branch of the APES in the PJTE case as well. We approximate the wrapped trough in terms of lower-order cubic harmonics  $V_4(\theta, \varphi)$  and  $V_6(\theta, \varphi)$ .

TABLE IV. Examples of  $M(3d^n)$  impurity ions with singlet ground states  $^{2S+1}A_{1g}$  or  $^{2S+1}A_{2g}$  in octahedral and cubic sites  $[MB_6]$  or  $[MB_8]$  (see Ref. [20]).

$d^n$	Dopant	High spin (weak field, small $e-t_2$ -splitting)		Low spin (strong field, large $e-t_2$ -splitting)	
		Configuration	Ground state	Configuration	Ground state
$d^0$	$Sc^{3+}, Ti^{4+}$		$^1A_{1g}$		$^1A_{1g}$
$d^3$	$V^{2+}, Cr^{3+}$	$(t_{2g}^* \uparrow)^3$	$^4A_{2g}$		$^4A_{2g}$ [21]
$d^5$	$Mn^{2+}, Fe^{3+}$	$(t_{2g}^* \uparrow)^3(e_g^* \uparrow)^2$	$^6A_{1g}$		
$d^6$	$Fe^{2+}, Co^{3+}$			$(t_2^* \uparrow)^3(t_2^* \downarrow)^3$	$^1A_{1g}$
$d^8$	$Ni^{2+}, Cu^{3+}$	$(t_{2g}^* \uparrow)^3(t_{2g}^* \downarrow)^3(e_g^* \uparrow)^2$	$^3A_{2g}$		$^3A_{2g}$ [21]
$d^{10}$	$Cu^+, Zn^{2+}$			$(t_2^* \uparrow)^3(t_2^* \downarrow)^3(e_g^* \uparrow)^2(e_g^* \downarrow)^2$	$^1A_{1g}$

By applying the modified Devonshire-O'Brien potential of Eq. (4), we employ its cubic symmetry and the essential property of parity. In the case of the JTE, inversion in the  $(\theta, \varphi)$  space changes the adiabatic ground-state wave function  $|0\rangle$  to that of the opposite sign. Therefore, in the adiabatic approximation, to avoid the ambiguity of the vibronic wave function, its nuclear factor must include the so-called Berry phase  $\varphi_B = \pi$  [10,31–34]. In the PJTE case, inversion in the  $(\theta, \varphi)$  space does not change the electronic wave function of the adiabatic approximation, and the Berry phase is zero  $\varphi_B = 0$ .

### C. Local vibronic dynamics and tunneling splitting of energy levels

In the tetrahedron site  $[\text{MB}_4]$  with the dominant vibronic coupling to the  $T_2$  mode and in the central-symmetric cases  $[\text{MB}_6]$  or  $[\text{MB}_8]$  with the coupling to the  $T_{1u}$  mode, the APES of the ground electron term has several symmetry-equivalent wells [5–10]. They transform into one another under the operations of the dopant-site symmetry group. If the wells are sufficiently deep, all the nuclear motion is randomly localized in one of the wells, where the dopant is off-center displaced. Alternatively, in the case of relatively low potential barriers, the atomic motion is reduced to tunneling between the wells or hindered rotations of the wave of low-symmetry distortion around the site. Although in all these cases the average value of the local dipole moment is zero, an applied electric field violates the equivalency of the wells. It localizes the off-center displacement of the dopant, producing a dipole moment at the dopant site. Accordingly, the dipole moment aligns with the applied electric field.

The local JTE-induced multiwell landscape of the lower branch of the APES with a wrapped trough in Eq. (4) preserves the overall tetrahedral (octahedral, cubic) symmetry of the site. For simplicity, in what follows, we assume that its orthorhombic potential barriers are significantly large, so the trigonal wells are sufficiently deep. In the tetrahedral case, the off-center positions of the dopant are at the bottom of wells  $a$ ,  $b$ ,  $c$ , and  $d$  [Fig. 4(a)], where the dopant-site symmetry is  $C_{3v}$ . At the bottom of the  $k$ th well, where  $\vec{r} = \vec{r}_k$  and the electronic ground-state wave function is  $|k\rangle$ , the Born-Oppenheimer ground state  $|k\rangle$  is an electron-vibrational product  $|k\rangle = |k\rangle\chi_0(\vec{r} - \vec{r}_k)$ . Due to the tetrahedral symmetry, for all  $k$  and  $j$  of the set  $a, b, c$ , and  $d$ , the overlap integrals and matrix elements of the Hamiltonian are equal:  $\langle k|H|j\rangle = \langle a|H|b\rangle = H_{ab}$ ,  $\langle k|j\rangle = \langle a|b\rangle = S_{ab} = S$  if  $k \neq j$ , and all  $\langle k|H|k\rangle = \langle a|H|a\rangle = H_{aa}$  if  $k = j$ . If the potential barriers are infinitely high, the ground-state nuclear motion is locked in one of the wells, and the ground state is fourfold degenerate [Fig. 4(b)]. In this basis of the four localized functions, the simplified JT Hamiltonian takes the following matrix form [35,36]:

$${}^4\mathbf{H}_{\text{JT}} = \Gamma(|a\rangle\langle b| + |a\rangle\langle c| + |a\rangle\langle d| + |b\rangle\langle c| + |b\rangle\langle d| + |c\rangle\langle d|) + \text{H.T.} \quad (5)$$

The left superscript indicates the order of the square matrix, and H.T. means Hermitian transpose.

Tunneling through finite-size barriers restores the broken tetrahedral symmetry  $C_{3v} \rightarrow T_d$ . The Born-Oppenheimer ground states  $|k\rangle$  form the basis of a reducible representation.

Tunneling lifts the fourfold degeneracy, yielding  $A_2 + T_1$  states [Fig. 4(b)]. Using symmetry projection, we transform the four Born-Oppenheimer ground states  $|k\rangle$  with  $k = a, b, c$ , and  $d$  to the four symmetry-adapted states [7,8,35–40],  $|A_2\rangle = \frac{1}{2}(|a\rangle + |b\rangle + |c\rangle + |d\rangle)$ ,  $|T_1\alpha\rangle = \frac{1}{2}(|a\rangle + |b\rangle - |c\rangle - |d\rangle)$ ,  $|T_1\beta\rangle = \frac{1}{2}(|a\rangle - |b\rangle + |c\rangle - |d\rangle)$ , and  $|T_1\gamma\rangle = \frac{1}{2}(|a\rangle - |b\rangle - |c\rangle + |d\rangle)$ . The respective energy levels are  $E_{A_2} = \langle A_2|H|A_2\rangle = (H_{aa} + 3H_{ab})/(1 + 3S) = E_0 + 3\Gamma$ , and  $E_{T_1} = \langle T_1\alpha|H|T_1\alpha\rangle = (H_{aa} - H_{ab})/(1 - S) = E_0 - \Gamma$ . Here,  $E_0 = \frac{1}{4}(E_{A_2} + 3E_{T_1}) \approx H_{aa}$ , and  $\Gamma = \frac{1}{4}(E_{A_2} - E_{T_1}) \approx H_{ab} - H_{aa}S$ . In what follows, we set the read-off mean-value energy of the ground state to zero. Then  $E(A_2) = 3\Gamma$ ,  $E(T_1) = -\Gamma$ , and the tunneling splitting energy gap is  $E(A_2) - E(T_1) \approx 4\Gamma$  [Fig. 4(b)].

Compared with the saddle points of the orthorhombic potential barriers, the conical intersection at  $\vec{r} = 0$  is high in energy,  $U_0(0) - U_0(C_{2v}) = \frac{3}{4}E_{\text{JT}}$ . For example, in the case of ZnO:  $\text{Ni}^{2+}$ , the potential barriers are  $\sim 360 \text{ cm}^{-1}$ . The conical intersection of the APES is sufficiently high in energy, and the excited vibronic states near this point become populated at the temperature close to (or above) 700 K. Therefore, at room temperature, the probability of a nuclear path traversing the trough through the conical intersection is negligible. Accordingly, such a path with the dopant crossing the center of the tetrahedron does not contribute to electric susceptibility. Instead, typical for the JTE, the leading source of orientation polarizability is the round motion from one trigonal minimum to another along the bottom of the wrapped trough, bypassing the conic intersection at  $\vec{r} = 0$ . Turning the dipole around the cone is easier under an electric field than moving the dopant through the center. Therefore, like polar liquids, solids with JTE centers possess orientation polarizability.

In a reasonable approximation, the slow angular motion along the wrapped trough follows the path of the steepest descent (the red curve in Fig. 3). In all perpendicular directions, the nuclear motions remain as small vibrations. This approximation reduces the multimode vibronic problem to the simple case of one-dimensional tunneling along the bottom of the wrapped trough. All the other degrees of freedom, being locally orthogonal to the path of steepest descent, are separated [38]. For the tunneling parameter  $\Gamma$ , the best result follows from the Wentzel-Kramers-Brillouin (WKB) approach [38,39], expressing the tunneling parameter  $\Gamma$  in terms of the tunneling integral along the path of steepest descent from the orthorhombic saddle point to the neighboring trigonal wells [7,38–40]:

$$\Gamma \approx 5\hbar\omega_0 \exp\left(-\frac{5E_{\text{JT}}}{4\hbar\omega_0}\right). \quad (6)$$

When  $\Gamma \lesssim \frac{1}{2}\hbar\omega_0$ , the JTE is moderate to strong. This condition translates into the inequality  $E_{\text{JT}} \gtrsim 2\hbar\omega_0$ . For example, in the case of ZnO:  $\text{Ni}^{2+}$ , using the above estimates, we have  $\hbar\omega_0 \approx 15 \text{ meV} \approx 121 \text{ cm}^{-1}$  and  $E_{\text{JT}} \approx 60 \text{ meV} \approx 480 \text{ cm}^{-1}$ , which indicates a strong JTE. From Eq. (7), in this case, we get  $\Gamma \approx 0.5 \text{ meV} \approx 4.0 \text{ cm}^{-1}$ .

The off-center shift of the dopant distorts the first coordination sphere. Its elastic and dipole-dipole electric interaction with the second coordination sphere causes a similar distortion to the next one. The distorted second sphere deforms the third one, etc. Though decreasing in magnitude with distance



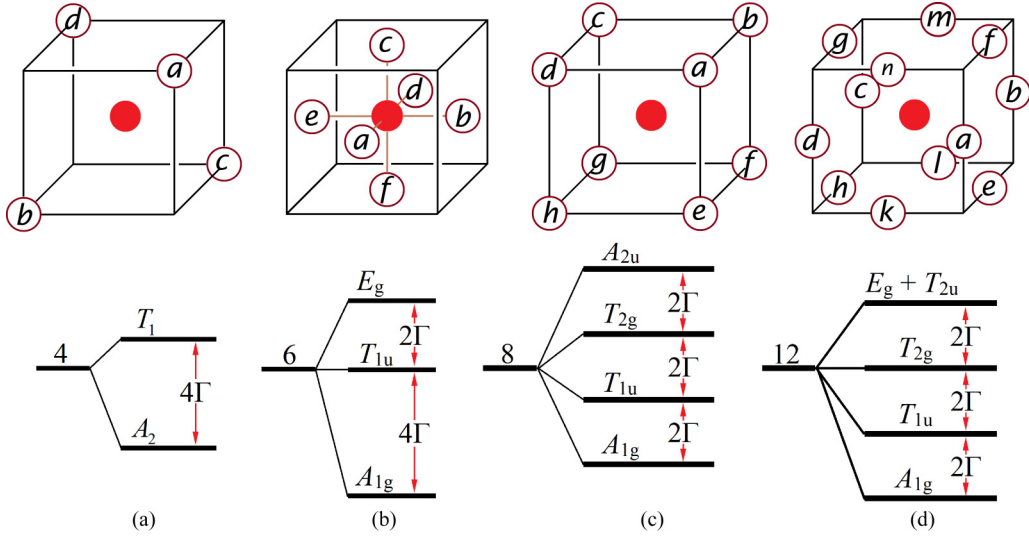


FIG. 5. Four cases of strong pseudo-Jahn-Teller effect (PJTE) with off-center instability and the corresponding tunneling splitting of the ground-state multiplet. (a) Trigonal wells in strong-coupling tetrahedral site with a PJTE  $(A_2 + T_1) \otimes t_2$ . (b)–(d) The 6-, 8-, and 12-well models in centrosymmetric sites  $[MB_6]$ ,  $[MB_8]$ , and  $[MB_{12}]$ , respectively.

from the dopant, this polaron-type crystal lattice distortion covers a vast region around the dopant site, contributing to an additional local polarization of the crystal [36]. As the local dipole rotates around the dopant site, it involves angular motion of all this polarized region of lattice distortion with an increased (dressed) rotational inertia.

As mentioned above, the landscape of the multimode APES is like that of the cluster  $[MB_4]$ . The number of wells and saddle points on its lower branch is the same as in the crystal-lattice multimode JTE [7]. Most importantly, in all these cases, there is just one tunneling path, the line of steepest descent (the red curve in Fig. 4). No matter how many vibrational modes are involved in the JTE, tunneling is a one-dimensional phenomenon. According to Eq. (5), one parameter  $E_{JT}/\hbar\omega_0$  determines the tunneling splitting of the corresponding energy levels. The qualitative similarity of the APES in the local and multimode cases provides the option of introducing the so-called *cluster model* [41], which treats the multimode impurity system as a molecule  $[MB_4]$ . After all but the tunneling degree of freedom are separated, no significant difference remains between the treatment of the crystal impurity problem and just the cluster  $[MB_4]$ , as the number of other degrees of freedom does not matter. We treat the vibronic coupling constant  $V$  and the bare frequency  $\omega_0$  of the cluster model as phenomenological parameters subject to further adjustment to the experimental data.

Employing the extended and somewhat modified Devonshire model for the cases of off-center instability in 6, 8, and 12 wells [35,36], we briefly list below the most important results regarding dipole tunneling in tetrahedral and cubic systems with the PJTE. Compared with the JTE, there is a substantial difference in applying the Devonshire model to the PJTE case. In the latter, inversion in the electronic space  $\{x, y, z\}$  does not change the sign of the adiabatic ground-state wave function  $|0\rangle$ . Therefore, opposite to the JTE case, if the ground electron state is an orbital singlet, the Berry phase is zero  $\varphi_B = 0$ ; therefore, the ground state is a

nondegenerate vibronic singlet. For example, for the tetrahedral cluster  $[MB_4]$  with a ground-state singlet term  $A_2$ , the PJTE for the quadratic  $(A_2 + T_1) \otimes t_2$  problem with relatively strong vibronic coupling to  $t_2$  modes results in trigonal wells on the lower branch of the APES, like the ones considered in Sec. III B. The corresponding tunneling states  $|A_2\rangle$ ,  $|T_1\alpha\rangle$ ,  $|T_1\beta\rangle$ , and  $|T_1\gamma\rangle$  are like those in the abovementioned case of the JTE, with the only difference in the order of the tunneling energy levels. The vibronic ground state in the PJTE problem is  $|A_2\rangle$  [Fig. 5(a)]. Therefore, the above consideration of the tunneling splitting in the JTE problem applies to the PJTE case, assuming that  $\Gamma$  is negative.

In centrosymmetric clusters  $[MB_6]$ ,  $[MB_8]$ , and  $[MB_{12}]$ , depending on the relative strength of higher-order vibronic coupling, the APES can have six tetragonal, eight trigonal, or 12 orthorhombic symmetry-equivalent wells [Figs. 5(b)–5(d)]. The tunneling dynamics in all these cases was considered by Gomez *et al.* [35]. In the case of six wells, the distance between diametrically distant minima  $a-d$ ,  $b-e$ , and  $c-f$  is greater than the distance between adjacent minima  $a-b$ ,  $b-d$ , etc. Therefore, the overlap integrals of the oscillator states in the corresponding wells are different in magnitude  $\langle\chi_0(\vec{r}-\vec{r}_a)|\chi_0(\vec{r}-\vec{r}_b)\rangle > \langle\chi_0(\vec{r}-\vec{r}_a)|\chi_0(\vec{r}-\vec{r}_d)\rangle$ . Including only the dominant contributions and setting the read-off mean-value energy to zero, we approximate the tunneling Hamiltonian by the following matrix  $6 \times 6$ :

$$\begin{aligned}
 {}^6\mathbf{H}_{\text{pJT}} = & -\Gamma(|a\rangle\langle b| + |a\rangle\langle c| + |a\rangle\langle e| + |a\rangle\langle f| + |b\rangle\langle c| \\
 & + |b\rangle\langle d| + |b\rangle\langle f|) - \Gamma(|c\rangle\langle d| + |c\rangle\langle e| \\
 & + |d\rangle\langle e| + |d\rangle\langle f| + |e\rangle\langle f|) + \text{H.T.} \quad (7)
 \end{aligned}$$

As above, the superscript indicates the order of the square matrix, and H.T. means Hermitian transpose. Like the case of four trigonal wells, the operator of symmetry projection transforms the six Born-Oppenheimer ground states  $|k\rangle$  to the six symmetry-adapted states  $|A_{1g}\rangle$ ,  $|T_{1u}\alpha\rangle$ ,  $|T_{1u}\beta\rangle$ ,  $|T_{1u}\gamma\rangle$ ,  $|E_g\theta\rangle$ , and  $|E_g\varepsilon\rangle$  that diagonalize the PJTE Hamiltonian in Eq. (8).

Its tunneling eigenvalues are  $E(A_{1g}) = -4\Gamma$ ,  $E(T_{1u}) = 0$ , and  $E(E_g) = 2\Gamma$ . Accordingly, the tunneling splitting is  $E(E_g) - E(A_{1g}) \approx 6\Gamma$  [Fig. 5(b)]. Similarly, in the case of eight trigonal

or 12 orthorhombic wells [Figs. 5(c) and 5(d)], neglecting the minor contributions, the tunneling Hamiltonians of the respective PJTE are as follows:

$$\begin{aligned}
 {}^8\mathbf{H}_{\text{pJT}} &= \Gamma(|a\rangle\langle b| + |a\rangle\langle d| + |a\rangle\langle e| + |b\rangle\langle c| + |b\rangle\langle f| + |c\rangle\langle d| + |c\rangle\langle g| + |d\rangle\langle h|) \\
 &\quad \times \Gamma(|e\rangle\langle f| + |e\rangle\langle h| + |f\rangle\langle g| + |g\rangle\langle h|) + \text{H.T.}, \\
 {}^{12}\mathbf{H}_{\text{pJT}} &= -\Gamma(|a\rangle\langle e| + |a\rangle\langle h| + |a\rangle\langle k| + |a\rangle\langle l| + |b\rangle\langle e| + |b\rangle\langle h| + |b\rangle\langle m| + |b\rangle\langle n|) \\
 &\quad - \Gamma(|c\rangle\langle f| + |c\rangle\langle g| + |c\rangle\langle m| + |c\rangle\langle n| + |d\rangle\langle f| + |d\rangle\langle g| + |d\rangle\langle k| + |d\rangle\langle l|) \\
 &\quad - \Gamma(|e\rangle\langle k| + |e\rangle\langle n| + |f\rangle\langle k| + |f\rangle\langle n| + |g\rangle\langle l| + |g\rangle\langle m| + |h\rangle\langle l| + |h\rangle\langle m|) + \text{H.T.}
 \end{aligned} \tag{8}$$

For details of the tunneling dynamics and the corresponding tunneling splitting energy-level diagram evaluation, see Gomez *et al.* [35].

#### IV. STARK EFFECT AND ORIENTATIONAL POLARIZATION OF THE JT DOPANT

As discussed in Sec. III A, due to the JTE problem  $T_1 \otimes t_2$  at each tetrahedral site of the  $[\text{MB}_4]$  cluster, the ground-state branch of the APES  $U_0(\vec{R})$  has symmetry-equivalent trigonal wells (Fig. 3), and in each well, the symmetry of the dopant site is lowered to trigonal  $T_d \rightarrow C_{3v}$  (Fig. 4). In the centrosymmetric cases  $[\text{MB}_6]$ ,  $[\text{MB}_8]$ , and  $[\text{MB}_{12}]$  with the PJTE  $(A_{1g} + T_{1u}) \otimes t_{1u}$  problem, the symmetry breaking in trigonal wells is  $O_h \rightarrow C_{3v}$ . Off-center distortion  $\vec{r}$  yields a local dipole moment  $\vec{p} = eZ_{\text{B}}\vec{r}/\sqrt{m^*} = p_0\vec{r}/R_0$ , where  $m^*$  is the effective mass of the local off-center mode, and  $R_0 = r_0\sqrt{3}$ , according to Eq. (3), is the radius of the trough, while  $p_0 = eZ_{\text{B}}R_0/\sqrt{m^*}$ . In the absence of an external electric field  $\vec{E} = 0$ , the wells are symmetry equivalent, providing for the resonance of the localized wave functions in the trigonal wells. Subject to the temperature population of the excited vibronic states, the JTE-induced nuclear motion (mainly that of the dopant ion) is either tunneling through orthorhombic barriers from one trigonal well to another or hopping over the potential barriers, realizing the hindered rotation. The dopant localization probability is spread evenly over the wells at the bottom of the two-dimensional trough of the APES. In each well, there is a nonzero polar distortion  $\vec{r} \neq 0$  with equal values  $|\vec{r}| = |\vec{r}_a| = |\vec{r}_b| = |\vec{r}_c| = |\vec{r}_d| = R_0 \neq 0$ , and the trigonal directions of  $\vec{r}$  are symmetry equivalent [Fig. 4(a)]. Therefore, the average dopant displacement is zero  $\langle \vec{r} \rangle = 0$ . The angular brackets stand for the temperature average over all the tunneling states under consideration  $\langle \vec{r} \rangle = \frac{1}{Z} \text{Tr}(e^{-\beta H} \vec{r})$ , with  $Z = \text{Tr}(e^{-\beta H})$  being the partition function, and  $\beta = 1/k_{\text{B}}T$ . As  $\vec{p} = p_0\vec{r}/R_0$ , the average dipole moment  $\langle \vec{p} \rangle$  is proportional to  $\langle \vec{r} \rangle$ . Therefore, at  $\vec{E} = 0$ , when  $\langle \vec{r} \rangle = 0$ , the average dipole moment is zero  $\langle \vec{p} \rangle = 0$  [Fig. 6(a)].

A nonzero electric field  $\vec{E} \neq 0$  applies a torque on each local dipole, turning it into alignment along  $\vec{E}$ . The dopant site acquires an induced dipole moment of nonzero magnitude  $\langle \vec{p} \rangle \neq 0$ . With the electric field removed, its value returns to zero due to thermal fluctuations. By definition, the polarization per site is the mean value of the induced electric dipole moment per unit volume  $\vec{P} = \langle \vec{p} \rangle/a^3$ , where  $a$  is the lattice constant. Thus, a nonzero electric field induces an orientational (non-displacive) polarization of the crystal  $\vec{P} \neq 0$ .

In the following section, we evaluate the nonzero average value of the dipole moment induced by the applied electric field in tetrahedral clusters  $[\text{MB}_4]$ . The electric field perturbation is  $W = -\vec{E} \cdot \vec{p} = -\vec{r}(p_0/R_0)$ . Consider relatively low temperatures  $k_{\text{B}}T \lesssim \hbar\omega_0$ . In this case, only the ground-state tunneling energy levels of Fig. 4(b) are temperature populated, and the contribution of all other excited states is negligible. Within the basis set of the four Born-Oppenheimer localized states  $|a\rangle$ ,  $|b\rangle$ ,  $|c\rangle$ , and  $|d\rangle$ , off-diagonal matrix elements of the dipole moment are proportional to the overlap integral  $\langle k|m \rangle$  and are negligibly small. Its diagonal matrix elements are proportional to the coordinates of the corresponding well  $\langle j|\vec{p}|j \rangle = (p_0/R_0)\langle j|\vec{r}|j \rangle = (p_0/R_0)\vec{r}_j$ , with  $\vec{r}_j$  from Eq. (3). Therefore, in this basis manifold, the dipole moment takes the following matrix form:  ${}^4\vec{p} = p_0(r_0/R_0){}^4\vec{\mathbf{D}}$ , where we introduce  $4 \times 4$  matrices  ${}^4\vec{\mathbf{D}} = ({}^4\mathbf{D}_x, {}^4\mathbf{D}_y, {}^4\mathbf{D}_z)$  representing the vector  $\vec{r}$  in this basis manifold. In each well, neglecting overlaps of Born-Oppenheimer states with other wells, these matrices are reduced to a diagonal form. For example, well  $b$  has coordinates  $r_0(1, -1, -1)$  [cf. Eq. (3)], and therefore,  $x_b = r_0\langle b|{}^4\mathbf{D}_x|b \rangle = r_0$ . In each trigonal well, the off-center shift of the dopant is  $R_0 = \sqrt{x^2 + y^2 + z^2} = r_0\sqrt{3}$ . Hence,  ${}^4\vec{p} = \frac{1}{\sqrt{3}}p_0{}^4\vec{\mathbf{D}}$  with the following diagonal matrices:

$$\begin{aligned}
 {}^4\mathbf{D}_x &= |a\rangle\langle a| + |b\rangle\langle b| - |c\rangle\langle c| - |d\rangle\langle d|, \\
 {}^4\mathbf{D}_y &= |a\rangle\langle a| - |b\rangle\langle b| + |c\rangle\langle c| - |d\rangle\langle d|, \\
 {}^4\mathbf{D}_z &= |a\rangle\langle a| - |b\rangle\langle b| - |c\rangle\langle c| + |d\rangle\langle d|.
 \end{aligned} \tag{9}$$

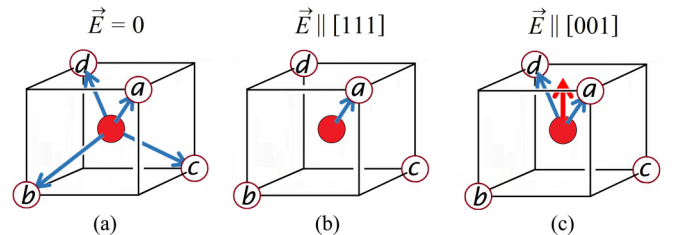


FIG. 6. Electric-field-induced dipole moments (blue arrows). (a) At zero field,  $\vec{E} = 0$ , the dopant is evenly distributed over the four trigonal wells, and the average value of the dipole moment is zero,  $\vec{p} = 0$ . (b) When  $\vec{E} \parallel [111]$ , well  $a$  lowers in energy, and the dopant is locked in this well with a nonzero dipole moment pointing in the same direction  $[111]$ . (c) When  $\vec{E} \parallel [001]$ , wells  $a$  and  $d$  are lower in energy, and the dopant is equally locked in these wells. The resultant average dipole moment  $\frac{1}{2}(\vec{p}_a + \vec{p}_d)$  is shown as red arrow.

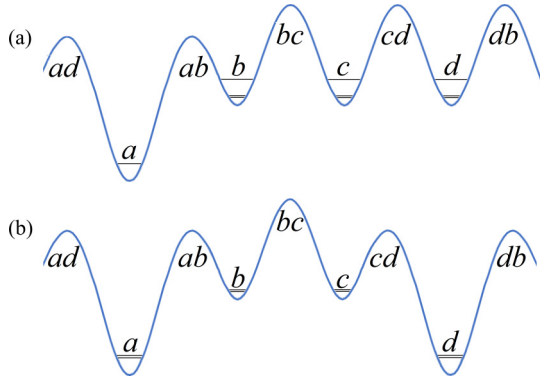


FIG. 7. One-dimensional cross-section along the path of steepest descent of the adiabatic potential energy surface (APES) of Fig. 3 distorted by a strong electric field. The four trigonal wells are labeled  $a$ ,  $b$ ,  $c$ , and  $d$ , [as in Fig. 4(a)], and the potential barriers between them are labeled  $ab$ ,  $bc$ ,  $cd$ ,  $ac$ ,  $ad$ , and  $bd$ , respectively. (a) Trigonal electric field,  $\vec{E} \parallel [1, 1, 1]$ , points toward well  $a$  [as in Fig. 6(b)], lowering well  $a$  and lifting the other three wells  $b$ ,  $c$ , and  $d$ . (b) Tetragonal field points along the  $z$  axis [as in Fig. 6(c)] lowering the adiabatic energy of wells  $a$  and  $d$  and lifting wells  $b$  and  $c$ .

### A. Orientational polarization at zero temperature

The applied electric field lowers the overall site symmetry, breaks the symmetry equivalence of the wells, and may destroy the resonance by locking the system in one trigonal well. For this to occur, the electric field should be greater than the critical value  $E_{cr} \approx \Gamma/p_0$ . Figure 7 gives a schematic illustration of its expected impact on the general landscape of the ground-state branch of the APES. Notably, this effect depends significantly on the strength of the JT coupling [7–10]. According to Eq. (3), the tunneling parameter  $\Gamma$  is exponentially small,  $\Gamma \propto \exp(-1.25E_{JT}/\hbar\omega_0)$ , and the dipole moment in the well is of the order of  $p_0 \propto \sqrt{(E_{JT}/\hbar\omega_0)}$ . Hence, in the case of a moderate-to-strong JTE, when  $E_{JT} \gtrsim 2\hbar\omega$ , the critical value of the electric field  $E_{cr} \propto \sqrt{(\hbar\omega_0/E_{JT})} \exp(-1.25E_{JT}/\hbar\omega)$  is relatively small. For example, in ZnO: Ni<sup>2+</sup>, assuming a moderate-to-strong JT coupling,  $E_{JT} \approx 480 \text{ cm}^{-1}$  and  $\hbar\omega_0 \approx 120 \text{ cm}^{-1}$ , Eq. (13) yields  $\Gamma \approx 4 \text{ cm}^{-1}$ . In this case, the off-center displacement of the Ni ion in the trigonal wells is about  $R_0\sqrt{3/m^*} \approx 0.27\text{\AA}$ . Accordingly, the field-induced dipole moment is  $eZ_B R_0\sqrt{3/m^*} \approx 15 \text{ D}$ . Therefore, to lock the system in a trigonal well, the critical value of the applied field should be at least  $\sim 15 \text{ kV/cm}$ , twice less than the dielectric strength of dry air.

Therefore, even a relatively weak electric field quenches the tunneling and locks the dopant in the field-oriented deepest well(s). The field-induced symmetry-breaking manifests itself as a nonzero polar distortion of the dopant site  $\langle \vec{r} \rangle \neq 0$ , and correspondingly, a field-induced nonzero dipole moment  $\langle \vec{p} \rangle = p_0 \langle \vec{r} \rangle / R_0$ . This rapid change from  $\langle \vec{p} \rangle = 0$  to its nonzero limiting value in trigonal well(s) implies an anomalously high value of its electric field derivative, meaning a giant susceptibility.

A relatively strong trigonal field  $\vec{E} = \frac{1}{\sqrt{3}}E(1, 1, 1)$ , with  $E > E_{cr}$ , pointing toward well  $a$ , lowers its energy and lifts the other three wells  $b$ ,  $c$ , and  $d$ . At

$k_B T = 0$ , only well  $a$  is temperature populated, while wells  $b$ ,  $c$ , and  $d$  are empty. Therefore, the mean value  $\langle \vec{r} \rangle \approx \vec{r}_a = \frac{1}{\sqrt{3}}R_0(1, 1, 1)$ , and the APES energy at its bottom drops:  $W_{[111]} = W_a = -\vec{E} \cdot \vec{p}_a = -\vec{E} \cdot \vec{r}_a(p_0/R_0) = -\frac{1}{\sqrt{3}}E(1, 1, 1) \cdot \frac{1}{\sqrt{3}}p_0(1, 1, 1) = -Ep_0$ , reaching the value  $|W_a| = Ep_0$  (Fig. 7). In wells  $b$ ,  $c$ , and  $d$ , where the vectors  $\vec{E}$  and  $\vec{p}$  are at the tetrahedral angle of  $109.5^\circ$  to one another, the adiabatic energy increases:  $W_b = W_c = W_d = -\frac{1}{\sqrt{3}}E(1, 1, 1) \cdot \frac{1}{\sqrt{3}}p_0(1, -1, -1) = \frac{1}{3}Ep_0$ . Hence, at  $T = 0 \text{ K}$ , when the only populated state is  $|a\rangle$ , the vector of induced dipole moment  $\langle \vec{p} \rangle \approx \vec{p}_a = \frac{1}{\sqrt{3}}p_0(1, 1, 1)$  is parallel to the electric field  $\vec{E}$ , and its magnitude is  $\langle p \rangle = |\vec{p}_a| = p_0$  [see Fig. 6(b)]. When  $\vec{E} = -\frac{1}{\sqrt{3}}E(1, 1, 1)$ , pointing opposite to well  $a$ , wells  $b$ ,  $c$ , and  $d$  drop in energy by  $\frac{1}{3}Ep_0$ , whereas the bottom of well  $a$  lifts up by the  $Ep_0$  value. Then at  $T = 0 \text{ K}$ , wells  $b$ ,  $c$ , and  $d$  are equally populated, whereas well  $a$  is empty. In this case, the average dipole moment is  $\langle \vec{p} \rangle \approx \frac{1}{3}(\vec{p}_b + \vec{p}_c + \vec{p}_d) = \frac{1}{3\sqrt{3}}p_0[(1, -1, -1) + (-1, 1, -1) + (-1, -1, 1)] = -\frac{1}{3\sqrt{3}}p_0(1, 1, 1)$ , with the magnitude of  $\langle p \rangle = \frac{1}{3}p_0$ .

When the vector of the applied electric field is in the tetragonal direction  $[001]$ , pointing to the midpoint of the edge of the tetrahedron between vertices 2 and 3,  $\vec{E} = E(0, 0, 1)$  [Fig. 6(c)], the trigonal wells  $a$  and  $d$  drop in energy,  $W_a = W_d = -E(0, 0, 1) \cdot \frac{1}{\sqrt{3}}p_0(1, 1, 1) = -\frac{1}{\sqrt{3}}Ep_0$ , whereas wells  $b$  and  $c$  move up in energy,  $W_b = W_c = \frac{1}{\sqrt{3}}Ep_0$  (Fig. 7). Therefore, at  $T = 0 \text{ K}$ , equally populated are the two wells  $a$  and  $d$ , with the nonzero mean value  $\langle \vec{r} \rangle \approx \frac{1}{2}(\vec{r}_a + \vec{r}_d) = \frac{1}{2\sqrt{3}}R_0[(1, 1, 1) + (-1, -1, 1)] = \frac{1}{\sqrt{3}}R_0(0, 0, 1)$ , whereas wells  $b$  and  $c$  are empty. Accordingly, the field-induced average dipole moment is in the same direction as the applied field  $\vec{E} = E(0, 0, 1)$ , and it takes the value of  $\langle \vec{p} \rangle = \frac{1}{\sqrt{3}}p_0$  [Fig. 6(c)].

At  $E > E_{cr}$ , no more significant changes in the induced value of the dipole moments occur. A stronger electric field can no longer increase the dipole moment when the system is locked in the lowest well. The direct influence of the electric field on the APES by shifting its wells is a weak second-order effect inversely proportional to the energy gap  $3E_{JT}$  between the branches of the APES. Accordingly, the field dependence of the induced polarization reaches a plateau. Comparing its varying maximum values  $\langle p \rangle_{\max}$  at different orientations of the electric field vector  $\vec{E}$ , we revealed a cubic anisotropy in the orientational polarization due to the local JTE.

Conversely, when  $E < E_{cr}$ , neglecting the electric field admixture of the tunneling singlet  $A_2$  to the ground-state tunneling triplet  $T_1$ , we can consider the Stark effect just in the  $T_1$  term [Fig. 4(b)]. When the applied electric field is trigonal  $\vec{E} = \frac{1}{\sqrt{3}}E(1, 1, 1)$ , the perturbation is  $W_{[111]} = -\vec{E} \cdot \vec{p} = -\frac{1}{\sqrt{3}}E(p_x + p_y + p_z)$ . Within the basis set of the three ground-state tunneling wave functions  $|T_1\alpha\rangle$ ,  $|T_1\beta\rangle$ , and  $|T_1\gamma\rangle$ , the perturbation  $W_{[111]}$  takes the form of a  $3 \times 3$  matrix. It splits the tunneling term  $T_1$  into a trigonal vibronic doublet  $\{|Eu\rangle, |Ev\rangle\}$  and a trigonal vibronic singlet  $|A_1\rangle$ , the latter being lower in energy [Fig. 4(c)]. The corresponding trigonal-field eigenvalues are  $W(A_1) = -\frac{2}{3}Ep_0$  and  $W(E)$

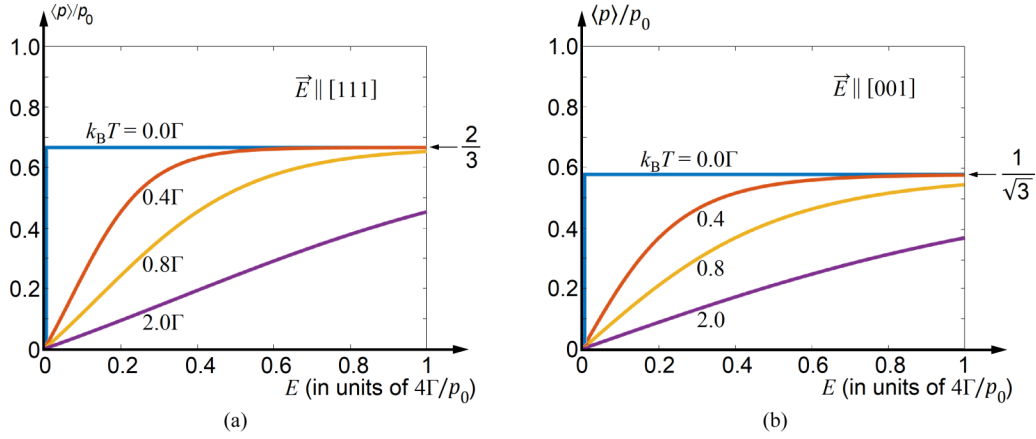


FIG. 8. Electric-field-induced dipole moment  $|\langle \vec{p} \rangle| = \langle p \rangle$  per one Jahn-Teller effect (JTE) site  $[\text{MB}_4]$  (in units of the dipole moment  $p_0$  in trigonal wells) vs the applied electric field (in units of  $4\Gamma/p_0$ ) at low temperatures,  $k_B T = 0, 0.04\Gamma, 0.08\Gamma$ , and  $0.16\Gamma$ , when the vibronic singlet is not populated. (a) The trigonal-field case,  $\vec{E} \parallel [111]$ . (b) The tetragonal-field case,  $\vec{E} \parallel [001]$ . In both cases, at  $k_B T = 0$ , there is a jump discontinuity in  $\langle p \rangle$ , from  $\langle p \rangle = 0$  at  $E = 0$  to  $\langle p \rangle = \text{const.} \cdot p_0$  at  $E \neq 0$  (shown in blue).

$= \frac{1}{3}E p_0$ . At  $T = 0$  K, populated is only the ground state  $|A_1\rangle = \frac{1}{\sqrt{3}}(|T_1\alpha\rangle + |T_1\beta\rangle + |T_1\gamma\rangle) = \frac{1}{2\sqrt{3}}(3|a\rangle - |b\rangle - |c\rangle - |d\rangle)$ . Therefore, the mean-value components of the dipole moment of Eq. (9) are the ground-state matrix elements  $\langle p_x \rangle = \langle A_1 | p_x | A_1 \rangle = \frac{2}{3\sqrt{3}}p_0$ ,  $\langle p_y \rangle = \langle A_1 | p_y | A_1 \rangle = \frac{2}{3\sqrt{3}}p_0$ , and  $\langle p_z \rangle = \langle A_1 | p_z | A_1 \rangle = \frac{2}{3\sqrt{3}}p_0$ . Hence, the magnitude of the vector is  $\langle p \rangle = \frac{2}{3}p_0$  [Fig. 8(a)]. Similarly, under a tetragonal electric field, when  $\vec{E} = E(0, 0, 1)$ , the tunneling term  $T_1$  splits into three tetragonal singlet states, the ground state being  $|u\rangle = \frac{1}{\sqrt{2}}(|T_1\alpha\rangle + |T_1\beta\rangle) = \frac{1}{\sqrt{2}}(|a\rangle - |d\rangle)$ . Accordingly, the mean-value components of the vector  $\langle \vec{p} \rangle$  are the ground-state matrix elements  $\langle p_x \rangle = \langle u | p_x | u \rangle = 0$ ,  $\langle p_y \rangle = \langle u | p_y | u \rangle = 0$ , and  $\langle p_z \rangle = \langle u | p_z | u \rangle = \frac{1}{\sqrt{3}}p_0 \approx 0.577p_0$ , so its magnitude is  $\langle p \rangle \approx 0.577p_0$  [Fig. 8(b)].

In Fig. 8, the horizontal line corresponds to the field dependence of  $\langle p \rangle$  at  $T = 0$  K, including the asymptote. Its numeric value is somewhat lower than the limiting value in Fig. 7. The reason is the lower flexibility of the linear combination of the three basis functions  $|T_1\alpha\rangle$ ,  $|T_1\beta\rangle$ , and  $|T_1\gamma\rangle$ . They cannot provide a complete localization of the ground state in just one well.

At  $E = 0$ , the symmetry of the dopant site is  $T_d$ , and as mentioned above, averaged over the degenerate components of the ground-state vibronic term, the mean value  $\langle p \rangle = 0$  [Fig. 6(a)]. When  $E \neq 0$ , the applied electric field reduces the symmetry of the dopant site to  $C_{3v}$  and lifts the degeneracy of the ground state. For example, any infinitesimally weak nonzero electric field along  $[111]$  lowers the minimum  $a$  with  $\vec{r} = \vec{r}_a$ . Hence, at  $T = 0$ , it induces a nonzero dipole moment  $\langle p \rangle \approx p_0$  [Fig. 6(b)], pointing in the same direction as the vector  $\vec{E}$ . Accordingly, there is a jump discontinuity in the value of the field-induced dipole moment from  $\langle p \rangle = 0$  at  $E = 0$  to  $\langle p \rangle \approx 0.67p_0$  in infinitesimally weak electric fields  $E \neq 0$  [Fig. 8(a)]. Accordingly, at  $E = 0$ , the field derivative of  $\langle \vec{p} \rangle$  is infinitely big; hence, when  $T = 0$ , the electric susceptibility has a singularity. Therefore, due to the nonzero Berry phase of the ground  $T_1$  term, this feature is characteristic of the

JTE. A similar zero-temperature jump discontinuity in  $\langle p \rangle$  at  $E = 0$  takes place under a tetragonal electric field with  $\vec{E} = E(0, 0, 1)$  [Fig. 8(b)].

Like the abovementioned case, a stronger electric field  $E \gtrsim E_{\text{cr}}$  splits the ground-state tunneling energy level  $T_1$  into a trigonal vibronic doublet  $\{|Eu\rangle, |Ev\rangle\}$  and a trigonal vibronic singlet  $|A_1\rangle$ . The latter is an invariant of the trigonal symmetry  $C_{3v}$ , the same as the excited tunneling singlet  $|A_2\rangle$ . Therefore, the nonzero matrix element  $\langle A_1 | W_{[111]} | A_2 \rangle \neq 0$  entangles the two singlet states. The corresponding eigenvalue problem for the  $2 \times 2$  matrix is easy to solve, and the respective mean values  $\langle p_x \rangle$ ,  $\langle p_y \rangle$ , and  $\langle p_z \rangle$  are easy to find, but the final expression for  $\langle p \rangle$  looks cumbersome. Instead, in Fig. 9(a), we provide the corresponding graph of its electric field dependence. As mentioned above, under a moderately strong electric field, no significant field-induced distortion of the APES is expected, and therefore, the graphs approach a plateau. For the tetragonal electric field  $\vec{E} = E(0, 0, 1)$ , a similar calculation can be performed, but the respective algebraic expression for  $\langle p \rangle$  is also awkward. Figure 9(b) gives an idea of the most essential features of its field dependence at relatively low temperatures.

The zero-temperature graph has a jump discontinuity at  $E = 0$  for both orientations of the applied electric field under consideration. Its physical meaning is the same as discussed above. When  $E = 0$ , the ground vibronic state is a three-fold degenerate tunneling term  $T_1$ , and for the perturbation  $W = -\vec{E} \cdot \vec{p}$ , averaged over its wave functions  $|T_1\alpha\rangle$ ,  $|T_1\beta\rangle$ , and  $|T_1\gamma\rangle$ , the resulting  $\langle W \rangle = 0$ . Any infinitesimally weak electric field  $E \neq 0$  breaks the cubic symmetry and, at zero temperature, averaged over the corresponding ground state, results in a nonzero finite value. In dopants with the PJTE for a nondegenerate electron state, the tunneling multiplet has a nondegenerate vibronic ground state. At  $k_B T = 0$ , it is the only temperature populated, and the corresponding mean value  $\langle W \rangle$  approaches zero with  $E \rightarrow 0$ . Therefore, in all the abovementioned cases of the PJTE, there is no jump discontinuity in  $\langle p \rangle$  and, correspondingly, no singularity in electric susceptibility at  $E = 0$ .

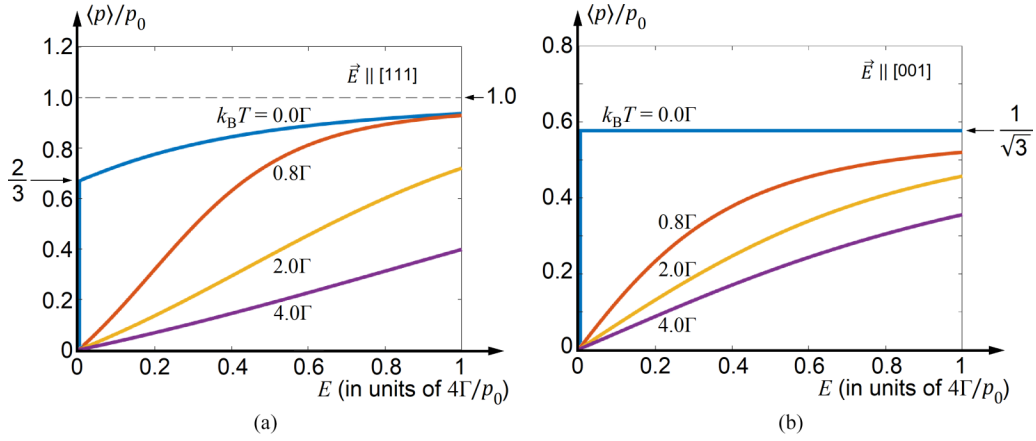


FIG. 9. Average value of the local dipole moment per one Jahn-Teller effect (JTE) site  $[MB_4]$  (in units of the dipole moment  $p_0$ ) vs the applied electric field (in units of  $4\Gamma/p_0$ ) at four different temperatures varying from very low  $k_B T = 0$  to relatively high  $k_B T = 4\Gamma$ . (a) Electric field is along trigonal direction  $\vec{E} = \frac{1}{\sqrt{3}}E(1, 1, 1)$ . The broken line is the horizontal asymptote at  $E \rightarrow \infty$ . (b) Tetragonal electric field  $\vec{E} = E(0, 0, 1)$ .

### B. Temperature dependence

The mean value of the dipole moment of a JTE site depends on the relative values of temperature  $k_B T$  and the JTE tunneling gap  $4\Gamma$ . The former determines the Boltzmann population of the Stark-effect split components of the tunneling multiplet, while the latter establishes the tunneling resistance of the JT site to the electric torque  $E p_0$ , tending to align the induced dipole with the applied electric field and lock it in the corresponding potential well. Increasing the applied electric field over the interval  $\Delta E_{cr} = E_{cr} \approx 4\Gamma/p_0$  increases the dipole moment  $\langle p \rangle$  from 0 to its maximum value  $p_0$ . Therefore, three energy parameters define the orientational polarizability: temperature  $k_B T$ , tunneling gap  $4\Gamma$ , and electric field strength  $E p_0$ , or equivalently, two dimensionless parameters  $\gamma = 4\Gamma/(k_B T)$  and  $\epsilon = E p_0/(k_B T)$ .

Consider low temperatures  $k_B T \ll 4\Gamma$ . The temperature population of the tunneling singlet state  $|A_2\rangle$  is negligible, and the dominant contribution to the electric-field-induced dipole moment is from the Stark effect in the ground-state tunneling triplet  $T_1$  [Fig. 4(b)]. All temperature effects are due to the Stark-effect-split components of the ground-state tunneling  $T_1$  term [Fig. 4(c)]. In the basis of the three symmetry-adapted states  $|T_1\alpha\rangle$ ,  $|T_1\beta\rangle$ , and  $|T_1\gamma\rangle$ , all components of the dipole moment are  $3 \times 3$  matrices  ${}^3\vec{p} = \frac{1}{\sqrt{3}}p_0({}^3\mathbf{D}_x, {}^3\mathbf{D}_y, {}^3\mathbf{D}_z)$ , where  ${}^3\mathbf{D}_x$ ,  ${}^3\mathbf{D}_y$ , and  ${}^3\mathbf{D}_z$  have the same form as  $\mathbf{C}_x$ ,  $\mathbf{C}_y$ , and  $\mathbf{C}_z$  in Eq. (2) but with opposite signs. Hence, the electric field perturbation  $W = -\vec{E} \cdot \vec{p}$  is also a  $3 \times 3$  matrix.

A trigonal field  $\vec{E} = \frac{1}{\sqrt{3}}E(1, 1, 1)$  pointing to well  $a$  splits the ground term  $T_1 \rightarrow A_1 + E$  into the ground-state trigonal singlet  $|A_1\rangle$ , dropping its energy to  $-\frac{2}{3}E p_0$ , and the trigonal vibronic doublet  $\{|Eu\rangle, |Ev\rangle\}$  at  $\frac{1}{3}E p_0$  [Fig. 4(c)]. The trigonal singlet  $|A_1\rangle = \frac{1}{2\sqrt{3}}(3|a\rangle - |b\rangle - |c\rangle - |d\rangle)$  includes a dominant contribution of the local state  $|a\rangle$  in well  $a$ . Hence, at low temperatures, it contributes most to the field-induced dipole moment. Orthogonal vibronic states of the trigonal vibronic doublet  $\{|Eu\rangle, |Ev\rangle\}$  dominantly include wells  $b$ ,  $c$ , and  $d$ . The corresponding dipole moment is

$$\langle p \rangle_{[111]} = \frac{2p_0}{3} \frac{1 - \exp(-\epsilon)}{1 + 2 \exp(-\epsilon)}. \quad (10)$$

Here, as above,  $\epsilon = E p_0/(k_B T)$ . With the increasing temperature population of the excited trigonal  $E$  term [Fig. 4(c)], the probability of finding the dopant spreads over these wells. Consequently, the field-induced polarization drops with temperature, as shown in Fig. 8(a).

Similarly, the tetragonal field  $\vec{E} = E(0, 0, 1)$  splits the ground-state tunneling vibronic term  $T_1$  into three tetragonal singlets  $|u\rangle$ ,  $|v\rangle$ , and  $|w\rangle$  with the energies  $-E p_0/\sqrt{3}$ ,  $E p_0/\sqrt{3}$ , and 0, respectively. In terms of  $\epsilon = E p_0/(k_B T)$ , the tetragonal dipole moment is

$$\langle p \rangle_{[001]} = \frac{p_0}{\sqrt{3}} \frac{1 - \exp(-2\epsilon/\sqrt{3})}{1 + \exp(-\epsilon/\sqrt{3}) + \exp(-2\epsilon/\sqrt{3})}. \quad (11)$$

At higher temperatures, with the growing population of the vibronic singlet  $A_2$  [Fig. 4(b)], all four tunneling states contribute to the electric-field-induced mean-value dopant displacement  $\langle \vec{r} \rangle$ . In the extended basis of the four symmetry-adapted states  $|A_2\rangle$ ,  $|T_1\alpha\rangle$ ,  $|T_1\beta\rangle$ , and  $|T_1\gamma\rangle$  with the operators  $p_x$ ,  $p_y$ , and  $p_z$  represented by  $4 \times 4$  matrices [cf. Eq. (9)], the electric field perturbation is also a  $4 \times 4$  matrix, and the angular brackets  $\langle \dots \rangle$  in  $\langle \vec{r} \rangle$  indicate the summation over all four vibronic states of the tunneling multiplet. Figure 10 displays the JTE-induced electric field dependence of the polarization  $\langle \vec{p} \rangle$  (in units of  $p_0$ ) per one dopant site. Both graphs follow from our numeric diagonalization of the Hamiltonian in Eq. (6) and the respective evaluation of  $\langle p_j \rangle$  with the electric field vector pointing in two characteristic directions  $\vec{E} || [111]$  and  $\vec{E} || [001]$ , at different temperatures, varying from very low at  $k_B T \approx 0$  to moderately high at  $k_B T \leq 4\Gamma$ . In all these cases, the orientational polarizability is maximal when the applied electric field points in one of the four trigonal directions along one of the wells, e.g.,  $\vec{E} || [111]$ . As mentioned above, at low temperatures under a strong electric field  $E > 4\Gamma/p_0$ , no further field-induced APES distortion is possible, and all the graphs approach a plateau. The broken line in Fig. 9(a) is the corresponding horizontal asymptote. Its numeric value and qualitative explanation are discussed above in Sec. IV A. For the tetragonal electric field  $\vec{E} = E(0, 0, 1)$ , comparing Figs. 8(b) and 9(b), we can see the tendency of a smoother

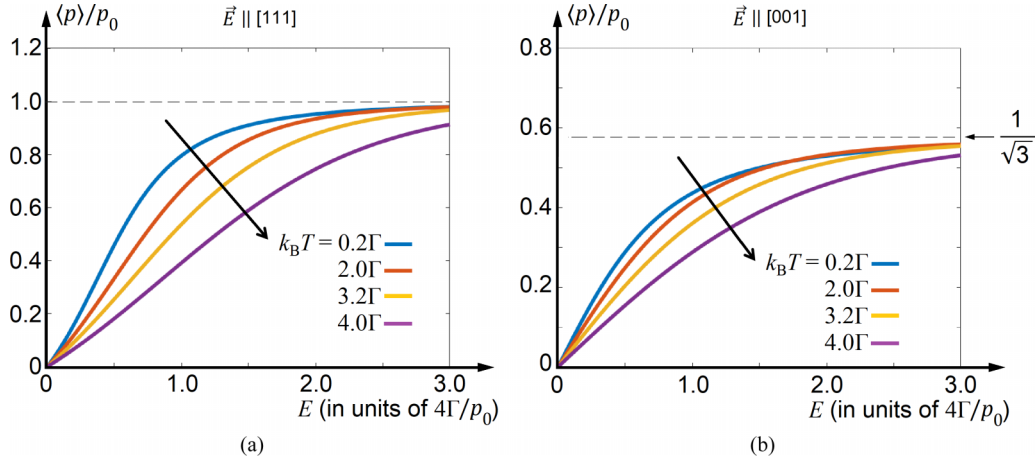


FIG. 10. Dipole moment of a tetrahedral cluster  $[MB_4]$  with the four-well pseudo-Jahn-Teller effect (PJTE) case  $(A_2 + T_1) \otimes t_2$  (in units of  $p_0$ ) vs the applied electric field (in units of  $4\Gamma/p_0$ ) at four different temperatures from  $k_B T = 0.2\Gamma$  to  $4\Gamma$ . Broken lines are horizontal asymptotes at  $E \rightarrow \infty$ . (a) The trigonal-field case  $\vec{E} \parallel [111]$ . (b) The tetragonal-field case  $\vec{E} \parallel [001]$ .

electric field dependence of  $\langle p \rangle$  at higher temperatures  $k_B T \approx 4\Gamma$ .

The numeric difference of the two graphs in Figs. 9(a) and 9(b) reveals a significant anisotropy in the angular dependence of  $\langle p \rangle$ . Distinguished from the regular case of tetrahedral sites with no JTE, where the electric polarizability is isotropic, the JTE creates a tetrahedral anisotropy. In this case, orientational polarizability is related to the crystal lattice symmetry axes. As expected, the polarization is at its maximum along trigonal directions when the electric field points toward one of the trigonal wells. Figure 11 shows the corresponding temperature-dependent angular diagram of polarization per dopant  $\langle p \rangle / p_0$ . It also indicates that the anisotropy smoothes out with temperature. This effect is due to the increasing temperature population of the vibronic singlet  $A_2$ , which is isotropic in its electric field response.

In this case, anisotropy of the polarization is related to the symmetry axes of the crystal and matches (approximately) a

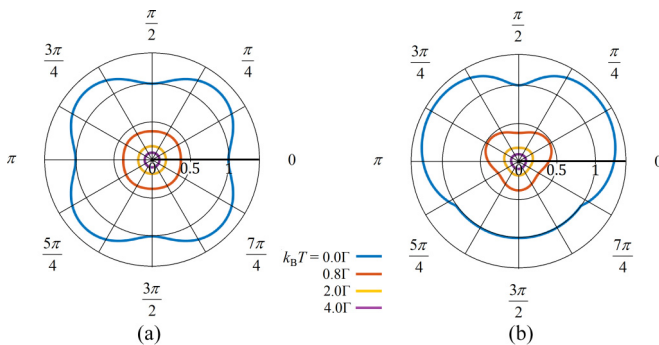


FIG. 11. Angular dependence of the dipole moment per one dopant site  $\langle p \rangle / p_0$  induced by the Jahn-Teller effect (JTE) problem  $T_1 \otimes t_2$  in a tetrahedral site  $[MB_4]$  under a strong electric field  $E = 2\Gamma/p_0$  at four different temperatures  $k_B T = 0, 0.8\Gamma, 2.0\Gamma$ , and  $4.0\Gamma$ , respectively. The concentric circles correspond to different values of  $\langle p \rangle / p_0$ . (a) Variation of  $\langle p \rangle / p_0$  in the equatorial cross-section plane  $z = 0$ , the latitude angle (measured from the equatorial plane)  $\theta = 0$ , and the azimuthal angle is  $0 < \varphi \leq 2\pi$ . (b) Variation of  $\langle p \rangle / p_0$  in the vertical cross-section plane at  $\varphi = \frac{1}{4}\pi$  vs the latitude angle  $\theta$ .

linear combination of tetrahedral invariants composed of the first cubic harmonics in terms of vector components of  $\vec{E}$ :

$$p(\vec{E}) \approx \frac{p_0}{4\Gamma E^3} [E^3 + (3 - \sqrt{3})E_x E_y E_z]. \quad (12)$$

In the PJTE case  $(A_2 + T_1) \otimes t_2$  with strong vibronic coupling, the tunneling ground state is a vibronic singlet  $A_2$  [Fig. 5(a)]. Therefore, as distinguished from the JTE case, due to the singlet nature of the ground state in the PJTE case, the field dependence of the polarization is smooth with no jump discontinuity at  $E = 0$ , varying from  $k_B T = 0$  to moderately high  $k_B T = 4\Gamma$  (Fig. 10). Like the JTE case, the numeric difference of the polarization  $\langle \bar{p} \rangle$  between the two directions of  $\vec{E} \parallel [111]$  and  $\vec{E} \parallel [001]$  indicates a significant anisotropy of polarizability depending on the orientation of the applied electric field. The corresponding angular dependence is like the one in Fig. 11.

Under strong electric fields, the difference in the electric properties of the JTE and PJTE sites as functions of their local induced dipole moments  $p_0$  is minor (but their  $p_0$  values may be significantly different). This similarity is due to the similar multivalley landscape of their APES and the corresponding polarization response discussed in Sec. IV A. For example, the strong-field asymptotes for the polarization in the four-well JTE case [Fig. 4(a)], four-well PJTE case [Fig. 5(a)], and eight-well PJTE case [Fig. 5(c)] are formally the same [42]. The polarization is maximal when the electric field points to one of the trigonal wells, lowering its energy and providing for its dominant thermal population. Like the tetragonal case of  $[MB_4]$ , in all the cases of the PJTE listed in Fig. 5, the high-temperature/low-field value of electric-field-induced polarization is isotropic and proportional to  $E p_0^2 / (k_B T)$ . Details are discussed below in Sec. V B.

## V. ORIENTATIONAL SUSCEPTIBILITY IN TETRAHEDRAL SITES WITH THE JTE

For a JT site in a relatively weak electric field, the magnitude of its field-induced dipole moment is proportional to the applied field  $\langle p_i \rangle = \varepsilon_0 \sum_j \chi_{ij} E_j$ , where  $\varepsilon_0$  is the vacuum

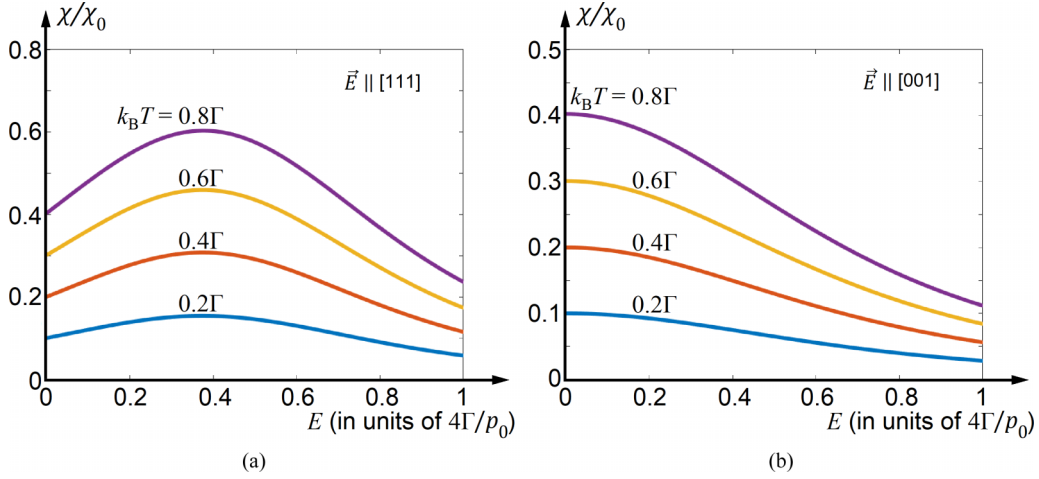


FIG. 12. Orientational susceptibility [in units of  $\chi_0$  of Eq. (20)] vs the applied electric field  $E$  (in units of  $4\Gamma/p_0$ ) in the four-well case of the pseudo-Jahn-Teller effect (PJTE) with the tunneling-level diagram shown in Fig. 5(a). The four graphs correspond to different temperatures  $k_B T = 0.2\Gamma, 0.4\Gamma, 0.6\Gamma$ , and  $0.8\Gamma$ . (a) Trigonal direction of the applied electric field  $\vec{E} \parallel [111]$ . (b) Tetragonal electric field  $\vec{E} \parallel [001]$ .

permittivity, and the linear factor; the tensor

$$\chi_{ij} = \frac{1}{\epsilon_0} \frac{\partial \langle p_i \rangle}{\partial E_j} \quad (13)$$

is the electric susceptibility per one site. Induced by the JTE, the rate of change of  $\langle p \rangle$  is of a rather significant magnitude on the order of  $\Delta \langle p \rangle / \Delta E \approx p_0 / E_{cr} = p_0^2 / (4\Gamma)$ . As it follows from the graphs in Fig. 9, decreasing the temperature to a value close to  $T = 0$  K reduces  $E_{cr}$  and increases the derivative  $p_0 / \Delta E_{cr}$  up to infinity at  $T \rightarrow 0$  K.

#### A. Low-temperature case

Consider the limit case of low temperatures  $k_B T \ll 4\Gamma$ . The temperature population of the tunneling singlet state  $|A_2\rangle$  is negligible, and the dominant contribution to the electric susceptibility is from the Stark effect in the ground-state tunneling triplet  $T_1$ .

As mentioned in Sec. IV A, the trigonal field  $\vec{E} = \frac{1}{\sqrt{3}}E(1, 1, 1)$  splits the term  $T_1$  into the ground-state trigonal singlet  $|A_1\rangle$  and the trigonal vibronic doublet  $\{|Eu\rangle, |Ev\rangle\}$ . Plugging the electric-field-induced dipole moment  $\langle p \rangle_{[111]}$  from Eq. (10) into Eq. (13), we find the corresponding susceptibility per one JT site:

$$\begin{aligned} \chi_{[111]} &= \frac{1}{\epsilon_0} \frac{\partial \langle p \rangle_{[111]}}{\partial E} = \frac{2p_0^2}{\epsilon_0 k_B T} \frac{\exp(-\epsilon)}{[1 + 2\exp(-\epsilon)]^2} \\ &= \chi_0 \frac{6\exp(-\epsilon)}{[1 + 2\exp(-\epsilon)]^2}, \end{aligned} \quad (14)$$

where as above in Sec. IV B,  $\epsilon = Ep_0/(k_B T)$  and  $\chi_0 = p_0^2/(3\epsilon_0 k_B T)$ . If in addition to low temperature the electric field is weak,  $Ep_0 \ll k_B T$ , so  $\epsilon$  approaches zero, then the fraction in Eq. (14) approaches  $\frac{2}{3}$ , and therefore, the trigonal susceptibility is

$$\chi_{[111]} = \frac{2}{3}\chi_0 \approx \frac{2p_0^2}{9\epsilon_0 k_B T}. \quad (15)$$

We thus come to the classical Langevin-Debye equation for the orientational polarizability of a polar liquid, vapor, or gas (e.g., see Ref. [43]):

$$\chi \approx \frac{p_{\text{eff}}^2}{3\epsilon_0 k_B T}, \quad (16)$$

with the effective dipole moment  $p_{\text{eff}} = p_0 \sqrt{\frac{2}{3}} \approx 0.82p_0$ .

Similarly, under a tetragonal field  $\vec{E} = E(0, 0, 1)$ , plugging the dipole moment  $\langle p \rangle_{[001]}$  from Eq. (11) into Eq. (13), we find the tetragonal susceptibility:

$$\begin{aligned} \chi_{[001]} &= \frac{1}{\epsilon_0} \frac{\partial \langle p \rangle_{[001]}}{\partial E} \\ &= \chi_0 \frac{\exp(-\epsilon/\sqrt{3}) + 4\exp(-2\epsilon/\sqrt{3}) + \exp(-3\epsilon/\sqrt{3})}{[1 + \exp(-\epsilon/\sqrt{3}) + \exp(-2\epsilon/\sqrt{3})]^2}, \end{aligned} \quad (17)$$

where as above,  $\epsilon = Ep_0/(k_B T)$  and  $\chi_0 = p_0^2/(3\epsilon_0 k_B T)$ . Under a relatively weak electric field, when  $Ep_0 \ll k_B T$  and  $\epsilon$  approaches zero, the fraction in Eq. (17) approaches  $\frac{2}{3}$ , and therefore, again,

$$\chi_{[001]} = \frac{2}{3}\chi_0 \approx \frac{2p_0^2}{9\epsilon_0 k_B T}, \quad (18)$$

with  $p_{\text{eff}} = p_0 \sqrt{\frac{2}{3}} \approx 0.82p_0$ . Also, the coincidence of  $\chi_{[111]}$  in Eq. (15) with  $\chi_{[001]}$  of Eq. (18) indicates isotropy of the weak-field susceptibility. Under the strong electric field, when  $\langle p_i \rangle \rightarrow p_{\text{max}}$  and the graph of the induced polarization reaches a plateau, its derivative, the electric susceptibility, drops to zero  $\chi_{ij} = \epsilon_0^{-1}(\partial \langle p_i \rangle / \partial E_j) \rightarrow 0$  (Fig. 12). This effect is due to the significant (almost complete) localization of the dopant in the corresponding well (Fig. 12).

#### B. Orientational susceptibility at relatively high temperatures

Assume the parameter  $\gamma = 4\Gamma/(k_B T)$  is small, meaning the temperature is relatively high  $k_B T > Ep_0$ , but  $k_B T < \hbar\omega$ , so the Boltzmann population of excited vibrational states in

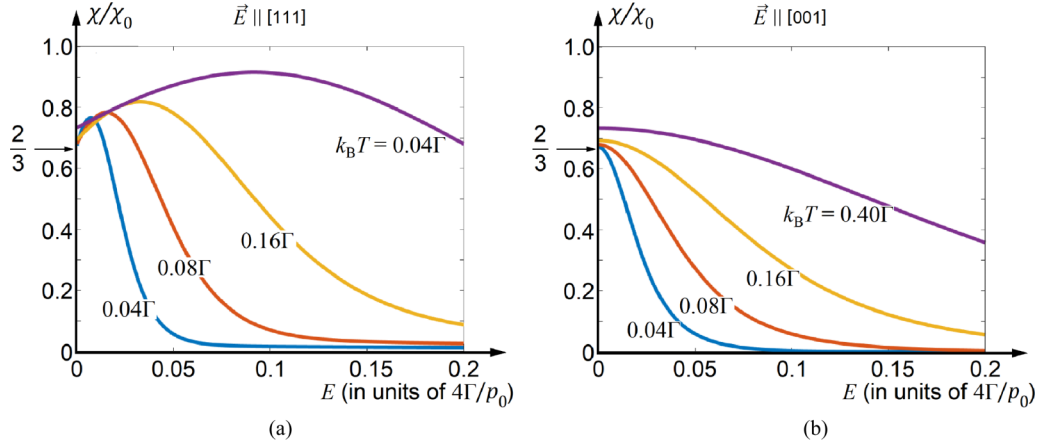


FIG. 13. Orientational susceptibility  $\chi$  per one Jahn-Teller (JT) site  $[\text{MB}_4]$  [in units of the Langevin-Debye susceptibility of Eq. (20)] vs the electric field  $E$  (in units of  $4\Gamma/p_0$ ) at relatively low temperatures  $k_B T = 0.04\Gamma, 0.08\Gamma, 0.16\Gamma$ , and  $0.4\Gamma$ . (a). The trigonal-field case  $\vec{E} \parallel [111]$ . (b). The tetragonal-field case  $\vec{E} \parallel [001]$ .

trigonal wells is neglectable. In this limit, all four vibronic states  $|T_1\alpha\rangle$ ,  $|T_1\beta\rangle$ ,  $|T_1\gamma\rangle$ , and  $|A_2\rangle$  of the ground tunneling multiplet contribute to  $\langle \vec{p} \rangle$ . The basis set includes just these four states, and the dipole moment is a  $4 \times 4$  vector matrix  $\frac{1}{\sqrt{3}}p_0(^4\mathbf{D}_x, ^4\mathbf{D}_y, ^4\mathbf{D}_z)$  including the  $4 \times 4$  matrices of Eq. (9). In a weak electric field, the ground states in the trigonal wells are close in energy. The system tunnels from one well to another or performs over-the-barrier hindered rotations in the warped two-dimensional trough. From the perturbation theory with the small parameter  $\epsilon = Ep_0/(k_B T)$ , we find

$$\frac{\partial \langle p_i \rangle_0}{\partial E_j} = \beta \int_0^1 \langle ^4\mathbf{p}_j(\tau) ^4\mathbf{p}_i \rangle_0 d\tau = \chi_0 \int_0^1 \langle ^4\mathbf{D}_j(\tau) ^4\mathbf{D}_i \rangle_0 d\tau, \quad (19)$$

with the  $4 \times 4$  matrices  $^4\mathbf{D}_j$  of Eq. (9), and as above,  $\chi_0 = p_0^2/(3\epsilon_0 k_B T)$ . The index 0 in  $\langle \dots \rangle_0$  means zero field  $E = 0$ ,  $^4\mathbf{D}_j(\tau) = \exp(\tau\beta H_{JT})(^4\mathbf{D}_j)\exp(-\tau\beta H_{JT})$  is the Heisenberg representation of the operator  $^4\mathbf{D}_j$ , and  $\beta = 1/k_B T$ . By symmetry, for  $i \neq j$ ,  $\langle ^4\mathbf{D}_j(t) ^4\mathbf{D}_i \rangle_0 = 0$ , and the diagonal components with  $i = j$  are all equal. Correspondingly, the electric susceptibility is isotropic (cf. the high-temperature angular diagram in Fig. 13), and the principal axes of the tensor  $\chi_{ij}$  have arbitrary orientation. Simplifying and integrating  $\langle ^4\mathbf{D}_j(t) ^4\mathbf{D}_i \rangle_0$  over  $\tau$ , we find

$$\int_0^1 \langle ^4\mathbf{D}_j(\tau) ^4\mathbf{D}_i \rangle_0 d\tau = \frac{2}{\gamma} \frac{\gamma + 1 - \exp(-\gamma)}{3 + \exp(-\gamma)} \delta_{ij}, \quad (20)$$

with  $\gamma = 4\Gamma/(k_B T)$ . Plugging Eq. (20) into Eqs. (19) and (13), we come to the isotropic weak-field limit for orientational susceptibility:

$$\chi = 2\chi_0 \frac{\gamma + 1 - \exp(-\gamma)}{\gamma[3 + \exp(-\gamma)]}. \quad (21)$$

At relatively slow tunneling, when  $4\Gamma < k_B T$  and  $\gamma$  approaches 0, the integral in Eq. (20) approaches the value of 1, and Eq. (21) simplifies to the Langevin-Debye equation with  $p_{\text{eff}} = p_0$ :

$$\chi \approx \chi_0 = \frac{p_0^2}{3\epsilon_0 k_B T}. \quad (22)$$

At  $T \rightarrow 0$  K, the value of  $\epsilon = Ep_0/(k_B T)$  is not small, and the approximated expressions in Eqs. (19)–(22) do not apply.

### C. Strong electric fields and/or high potential barriers $Ep_0 \geq 4\Gamma$

When the potential barriers are relatively high, the tunneling frequency is low, and the tunneling parameter  $\Gamma$  is small. Most of the time, the dopants are in one of the four trigonal wells. A relatively strong electric field  $E \gtrsim 4\Gamma/p_0$  destroys the resonance of the localized states in the wells and locks the dopants in the deepest well(s) (Fig. 7). Corresponding to the graphs in Fig. 9, induced by strong electric fields, the magnitude of the dipole moment reaches a plateau  $\langle p_i \rangle \rightarrow p_{\text{max}}$ , with the value of  $p_{\text{max}}$  determined by the site dipole moment at the bottom of the deepest well, per the qualitative reasoning illustrated in Fig. 7. When the dopant is locked in one of the wells, its orientational motion is entirely exhausted, and the orientational polarization no longer depends on the applied field. The deeper the potential wells, the more rigid the JT site becomes. Correspondingly, under strong electric fields  $E \gtrsim 4\Gamma/p_0$ , the derivative  $\chi_{ij} = \epsilon_0^{-1}(\partial \langle p_i \rangle / \partial E_j)$  approaches zero (Figs. 12 and 14).

### D. Arbitrary values of temperature and electric fields

According to Eq. (13), accurate values of the electric susceptibility result from the numeric differentiation of the dopant polarization with respect to  $E$  (Fig. 15). Its low-temperature peak value is due to the singularity of  $\langle p \rangle$  at  $E = 0$  discussed in Secs. IV A and IV B. Under a strong electric field, according to Figs. 9 and 11, the polarization approaches its asymptotic value, and the electric field dependence levels to a plateau. Accordingly, in this case, as shown in Figs. 13 and 15, the derivative of  $\langle p \rangle$  approaches zero. The lower the temperature, the faster the electric susceptibility drops to zero.

The difference in numeric values of the electric susceptibility in Figs. 13(a) and 13(b) in the two characteristic directions of the applied electric field, the trigonal vs tetragonal, indicates significant angular dependence of the orientational susceptibility, which is not expected in a cubic crystal with no JTE. Induced by the latter, the susceptibility is maximal along



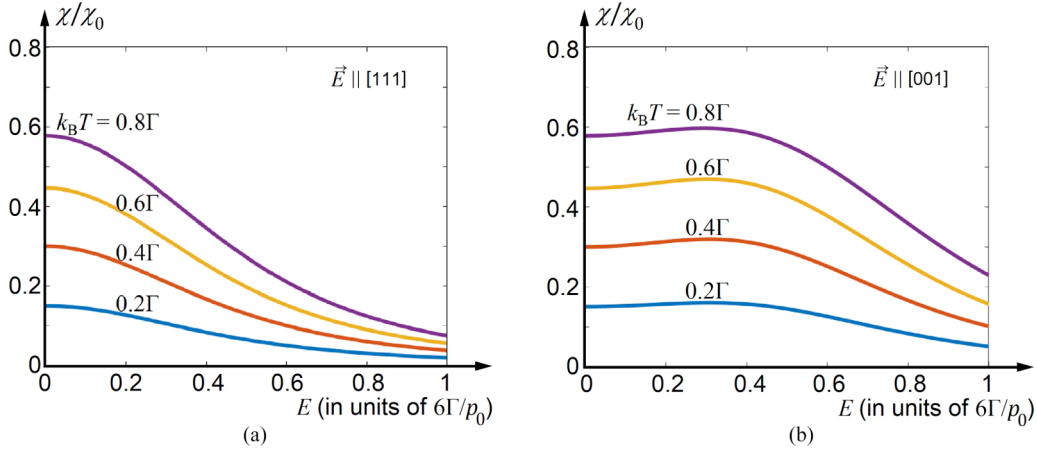


FIG. 14. The six-well case of the pseudo-Jahn-Teller effect (PJTE) with the tunneling-level diagram shown in Fig. 5(b). Orientational susceptibility vs the applied electric field  $E$  (in units of  $6\Gamma/p_0$ ). The four graphs correspond to different temperatures  $k_B T = 0.3\Gamma$ ,  $0.6\Gamma$ ,  $0.9\Gamma$ , and  $0.8\Gamma$ . (a). Trigonal direction of the applied electric field  $\vec{E} \parallel [111]$ . (b). Tetragonal electric field  $\vec{E} \parallel [001]$ .

the trigonal axes, where the absolute minima reside, while the smallest value of  $\chi$  emerges along the highest tetragonal saddle points of the APES (cf. Fig. 3). Linked to the symmetry axes of the crystal, this anisotropy (approximately) matches a linear combination of tetrahedral invariants composed of the first cubic harmonics in terms of vector components of  $\vec{E}$ . When the electric field vector  $\vec{E}$  points along one of the symmetry directions of the cubic crystal, the vector of polarization is parallel to the vector  $\vec{E}$ .

## VI. ORIENTATIONAL SUSCEPTIBILITY IN SOLIDS WITH PJTE

In the case of a strong-coupling PJTE problem ( $A_2 + T_1$ )  $\otimes t_2$  [or ( $A_1 + T_2$ )  $\otimes t_2$ ] for an electron singlet ground state  $A_2$  (or  $A_1$ ) in tetrahedral dopant sites [ $MB_4$ ], the lowest branch of the APES can also have a trough with off-center shifted trigonal wells (see above Sec. III). Shown in Fig. 5(a), the respective energy-level diagram of the ground-state tunneling multiplet looks like the one in the JTE case ( $T_1 + A_2$ )  $\otimes t_2$

of Fig. 4(b), but with inverted energy levels. Changing the sign of  $\Gamma$  in Eq. (21), we find the low-field/high-temperature expression for isotropic susceptibility in this case:

$$\chi = 2\chi_0 \frac{1 + (\gamma - 1) \exp(-\gamma)}{\gamma[1 + 3 \exp(-\gamma)]}, \quad (23)$$

with  $\gamma = 4\Gamma/(k_B T)$  and  $\chi_0$  of Eq. (20).

In the high-temperature limit, when  $k_B T \ll 4\Gamma$ , meaning  $\gamma$  approaches zero, the fraction in the expression in Eq. (21) approaches  $\frac{1}{2}$ , and therefore,  $\chi$  in Eq. (21) simplifies to  $\chi_0$ , the Langevin-Debye Eq. (16) with the effective dipole moment  $p_{\text{eff}} = p_0$ . In the opposite case of low temperatures  $k_B T \ll 4\Gamma$ , the thermal population of the tunneling triplet is neglectable, while in the ground-state tunneling singlet, there is no first-order Stark effect. Therefore, the field-induced electric dipole moment is zero  $\langle \vec{p} \rangle = 0$ . Accordingly, at  $T \rightarrow 0$  K, its derivative, the orientational susceptibility approaches zero  $\chi \rightarrow 0$ .

Accurate values of the orientational susceptibility follow from the numeric differentiation of the electric field

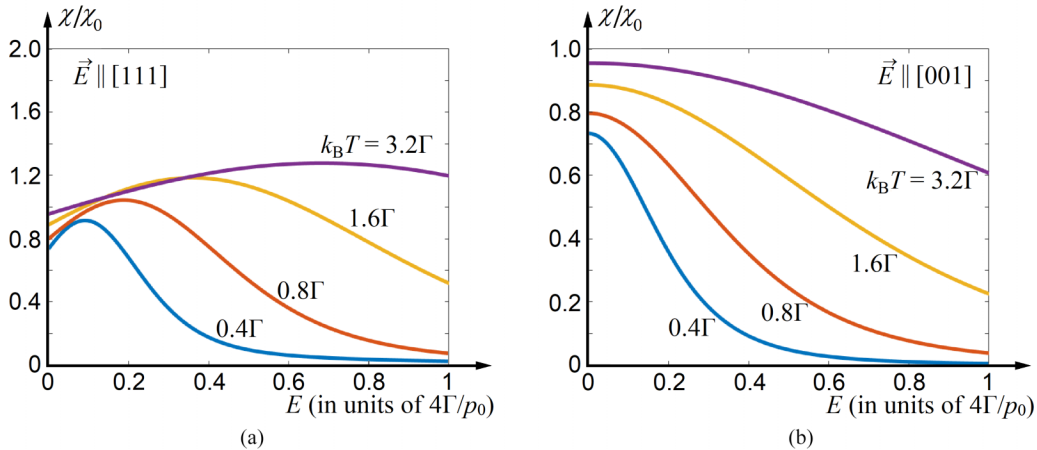


FIG. 15. Orientational susceptibility  $\chi$  per one Jahn-Teller (JT) site [ $MB_4$ ] [in units of the Langevin-Debye susceptibility of Eq. (20)] vs the electric field  $E$  (in units of  $4\Gamma/p_0$ ) at relatively high temperatures  $k_B T = 0.4\Gamma$ ,  $0.8\Gamma$ ,  $1.6\Gamma$ , and  $3.2\Gamma$ . (a) The trigonal-field case  $\vec{E} \parallel [111]$ . (b) The tetragonal-field case  $\vec{E} \parallel [001]$ .

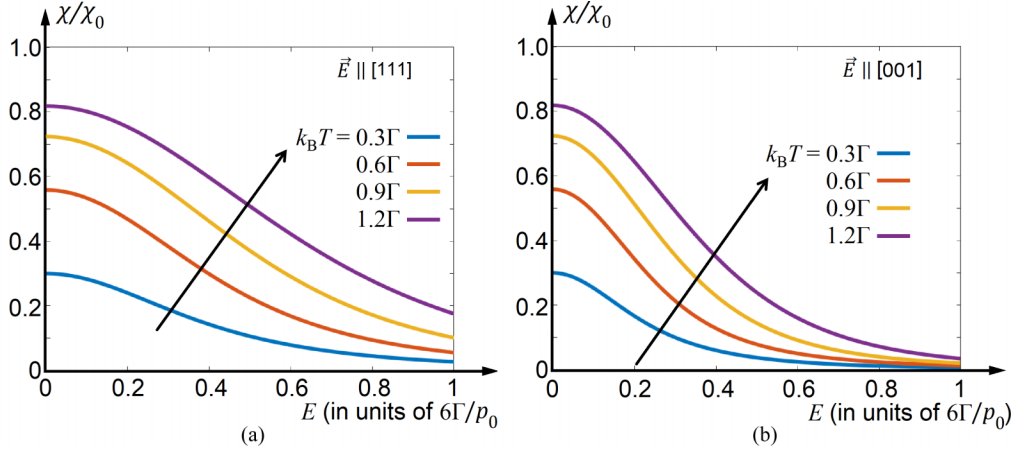


FIG. 16. Orientational susceptibility vs the applied electric field  $E$  (in units of  $6\Gamma/p_0$ ) for the eight-well case of the pseudo-Jahn-Teller effect (PJTE) with the tunneling-level diagram shown in Fig. 5(c). The four graphs correspond to different temperatures  $k_B T = 0.3\Gamma$ ,  $0.6\Gamma$ ,  $0.9\Gamma$ , and  $0.8\Gamma$ . (a) Under the trigonal field  $\vec{E} \parallel [111]$ . (b) In the tetragonal field  $\vec{E} \parallel [001]$ .

dependence of polarization in Fig. 10 with respect to the applied field. In Fig. 12, we show the electric field dependence of the electric susceptibility of the tetrahedral PJTE dopant site  $[MB_4]$  with strong coupling  $(A_2 + T_1) \otimes t_2$  [or  $(A_1 + T_2) \otimes t_2$ ] case and the four-well APES of Fig. 5(a). The orientational polarizability of the site with the PJTE increases with temperature. This property is due to the inverted energy-level diagram in Fig. 5(a) compared with the one in Fig. 4(b). With only the ground-state tunneling singlet populated at  $T = 0$  K, there is no linear Stark effect at the PJTE site, yielding zero susceptibility. With the increase in temperature, the Boltzmann population of the excited-state tunneling triplet adds up, increasing its nonzero contribution to susceptibility.

In what follows, we briefly describe orientational susceptibility in other cases of the PJTE listed in Fig. 5. In the six-well case shown in Fig. 5(b), within the basis of the manifold of six states  $|a\rangle$ ,  $|b\rangle$ ,  $|c\rangle$ ,  $|d\rangle$ ,  $|e\rangle$ , and  $|f\rangle$  localized in the wells, the dipole moment  $\vec{p} = p_0 \vec{r}/R_0$  takes the following matrix form:

${}^6\vec{p} = p_0({}^6\mathbf{D}_x, {}^6\mathbf{D}_y, {}^6\mathbf{D}_z)$  with diagonal  $6 \times 6$  matrices:

$$\begin{aligned} {}^6\mathbf{D}_x &= |a\rangle\langle a| - |d\rangle\langle d|, \\ {}^6\mathbf{D}_y &= |b\rangle\langle b| - |e\rangle\langle e|, \\ {}^6\mathbf{D}_z &= |c\rangle\langle c| - |f\rangle\langle f|, \end{aligned} \quad (24)$$

representing the coordinates of the dopant  $x$ ,  $y$ , and  $z$  in this basis manifold. Combining the Hamiltonian  ${}^6\mathbf{H}_{\text{PJTE}}$  of Eq. (7) with the perturbation  ${}^6\mathbf{W} = -\vec{E} \cdot {}^6\vec{p}$ , we find the electric field dependence of the orientational susceptibility for a PJTE site with the six-well APES (Fig. 14). As above, the reference value  $p_0$  of the dipole moment corresponds to the dopant off-center displacement in any of the six wells.

A detailed consideration of the PJTE  $(A_{1g} + T_{2u}) \otimes t_{2u}$  resulting in the eight-well APES [Fig. 5(c)] is available in Ref. [42]. In the basis manifold of eight localized wave functions  $|a\rangle$ ,  $|b\rangle$ ,  $|c\rangle$ ,  $|d\rangle$ ,  $|e\rangle$ ,  $|f\rangle$ ,  $|g\rangle$ , and  $|h\rangle$ , the dipole moment is the vector  ${}^8\vec{p} = \frac{1}{\sqrt{3}} p_0({}^8\mathbf{D}_x, {}^8\mathbf{D}_y, {}^8\mathbf{D}_z)$  with the following diagonal matrices  $8 \times 8$ :

$$\begin{aligned} {}^8\mathbf{D}_x &= |a\rangle\langle a| - |b\rangle\langle b| - |c\rangle\langle c| + |d\rangle\langle d| + |e\rangle\langle e| - |f\rangle\langle f| - |g\rangle\langle g| + |h\rangle\langle h|, \\ {}^8\mathbf{D}_y &= |a\rangle\langle a| + |b\rangle\langle b| - |c\rangle\langle c| - |d\rangle\langle d| + |e\rangle\langle e| + |f\rangle\langle f| - |g\rangle\langle g| - |h\rangle\langle h|, \\ {}^8\mathbf{D}_z &= |a\rangle\langle a| + |b\rangle\langle b| + |c\rangle\langle c| + |d\rangle\langle d| - |e\rangle\langle e| - |f\rangle\langle f| - |g\rangle\langle g| - |h\rangle\langle h|. \end{aligned} \quad (25)$$

Combining the Hamiltonian  ${}^8\mathbf{H}_{\text{PJTE}}$  of Eq. (8) with the electric field perturbation  ${}^8\mathbf{W} = -\vec{E} \cdot {}^8\vec{p}$ , we find the average values of the field-dependent components  $\langle p_i \rangle$  of the induced dipole moment and their related field derivatives (Fig. 16).

Similarly, in the case of a 12-well APES shown in Fig. 5(d), the basis manifold includes 12 ground-state localized wave functions  $|a\rangle$ ,  $|b\rangle$ ,  $|c\rangle$ ,  $|d\rangle$ ,  $|e\rangle$ ,  $|f\rangle$ ,  $|g\rangle$ ,  $|h\rangle$ ,  $|k\rangle$ ,  $|l\rangle$ ,  $|m\rangle$ , and  $|n\rangle$ , and the dipole moment is  ${}^{12}\vec{p} = \frac{1}{\sqrt{2}} p_0({}^{12}\mathbf{D}_x, {}^{12}\mathbf{D}_y, {}^{12}\mathbf{D}_z)$  with the diagonal matrices:

$$\begin{aligned} {}^{12}\mathbf{D}_x &= |a\rangle\langle a| - |b\rangle\langle b| - |c\rangle\langle c| + |d\rangle\langle d| + |k\rangle\langle k| + |l\rangle\langle l| - |m\rangle\langle m| - |n\rangle\langle n|, \\ {}^{12}\mathbf{D}_y &= |a\rangle\langle a| + |b\rangle\langle b| - |c\rangle\langle c| - |d\rangle\langle d| + |e\rangle\langle e| - |f\rangle\langle f| - |g\rangle\langle g| + |h\rangle\langle h|, \\ {}^{12}\mathbf{D}_z &= |e\rangle\langle e| + |f\rangle\langle f| - |g\rangle\langle g| - |h\rangle\langle h| + |k\rangle\langle k| - |l\rangle\langle l| - |m\rangle\langle m| + |n\rangle\langle n|. \end{aligned} \quad (26)$$

Combining the Hamiltonian  ${}^{12}\mathbf{H}_{\text{PJTE}}$  of Eq. (8) with the perturbation  ${}^{12}\mathbf{W} = -\vec{E} \cdot {}^{12}\vec{p}$ , we find the electric field dependence of the orientational susceptibility for this case shown in Fig. 17.

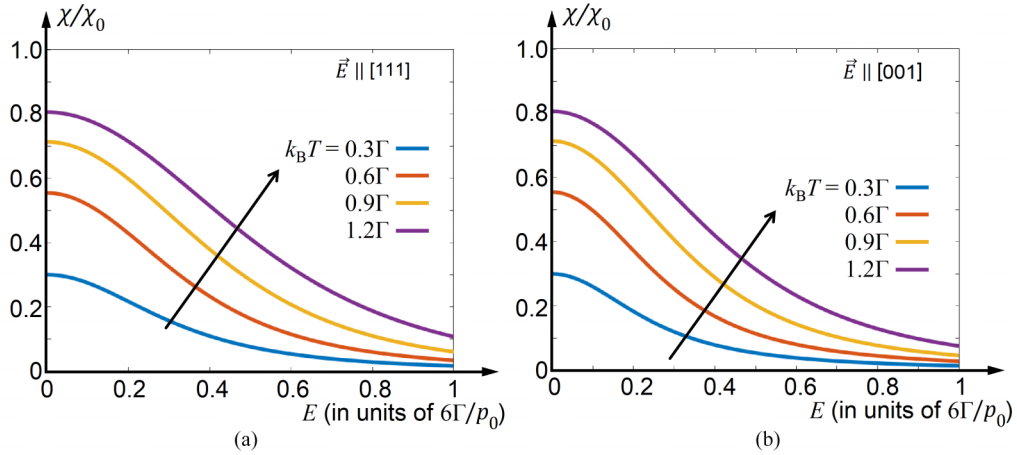


FIG. 17. Same as in Fig. 16 for pseudo-Jahn-Teller effect (PJTE) with the 12-well adiabatic potential energy surface (APES) as in Fig. 5(d). Although the graphs in both (a) and (b) look like the respective ones in Figs. 16(a) and 16(b), they drop to zero with  $E$  somewhat faster than in Fig. 16.

The qualitative reasoning illustrated in Fig. 7 also applies to all PJTE cases with a multiwell APES. If the electric field is sufficiently strong, it destroys the symmetry of the wells and quenches tunneling, like the JTE case. Under a strong electric field, the graph of the induced polarization reaches a plateau. Consequently, the orientational susceptibility approaches zero  $\chi_{ij} \rightarrow 0$ . In all PJTE cases, the ground vibronic state is a tunneling singlet (cf. Fig. 5), meaning there is no first-order Stark effect at  $T = 0$  K when the temperature population of all the excited states is zero. Therefore, orientational susceptibility in all these cases is close to zero. With increasing temperature, the population of the excited components of the tunneling multiplet increases. They are subject to the first-order Stark effect, increasing the orientational susceptibility of the PJTE site, as shown in Figs. 12, 14, 16, and 17. Since the ground tunneling state of all the PJTE cases is a vibronic singlet, there is no singularity at  $T = 0$  K in the field dependence of the polarization, as in the JTE case (Sec. IV). Therefore, for a system with the PJTE, the orientational susceptibility is significantly weaker at low temperatures [42].

## VII. DISCUSSION OF THE RESULTS

Oriental susceptibility in solids is among solid-state properties resulting from the dipolar instabilities and distortions induced by the JTE and PJTE. Revealed [2] due to the PJTE in  $\text{BaTiO}_3$ , rotating local dipoles at the titanium centers were shown to be the origin of the formation of the four phases of this crystal, one paraelectric and three ferroelectric, and the order-disorder transitions between them [16,17,42,44]. This discovery was an indication of the feasibility of Debye's [1] hypothesis of the possible existence of free-orienting dipoles in solids, which he mentioned long before the finding of ferroelectricity. Obviously, after revealing the mobile dipoles in solids, which explain the origin of the ferroelectric phases in centrosymmetric crystals, the following steps were made by analyzing the properties of such systems in interaction with external perturbations, showing that (among other properties) it leads to multiferroicity [17,29], giant flexoelectricity [17,44], permittivity [17,42,44], and electrostriction [44].

This property of orientational susceptibility is among characteristic features in all the solids where dipolar distortions may take place as a consequence of the JTE in noncentrosymmetric systems (symmetry group  $T_d$ ,  $T_h$ ,  $D_{2d}$ , or  $C_{3v}$ ) or as a PJTE in systems with an inversion center (e.g.,  $\text{BaTiO}_3$  [2,7,8,16,44]). The results of this paper for the susceptibility of cubic sites may be regarded as a general virtual property of any solid-state system with JTE- or PJTE-induced dipolar instabilities.

### A. The model

The calculations consider a small-radius dopant in a tetrahedral site with the JTE in the ground-state orbital triplet and a central-symmetric cubic or octahedral site with the PJTE in the orbital singlet state deep in the band gap of an insulator or a wide-gap semiconductor. The so-called cluster model assumes its coupling to vibrations of only the first coordination sphere of the anion ligands. The tight-binding approach to a relatively compact  $3d$  shell justifies the small-radius impurity approximation, and it is approximately valid for many transition-metal dopants (see Tables II–IV). The spin multiplicity of the impurity term is less important here, provided the spin-orbital coupling is not strong enough to quench the JTE or PJTE. Examples of wide-gap crystals with cubic sphalerite or hexagonal wurtzite structures are plenty, e.g., some of the  $A^{\text{III}}B^{\text{V}}$  semiconductors,  $\text{ZnO}$ ,  $\text{ZnS}$ ,  $\text{ZnSe}$ , and  $\text{ZnTe}$ , or of the  $A^{\text{II}}B^{\text{VI}}$  type, e.g.,  $\text{GaP}$  or  $\text{AlP}$ . In all such systems, the relatively strong JT coupling of their electronic  $^{2S+1}T$  terms with the environment may contribute significantly to their polarizability, in addition to the metal sites with a singlet ground state  $^{2S+1}A_1$  and a relatively strong PJTE like in the abovementioned cubic perovskites such as  $\text{BaTiO}_3$  and off-center impurities, with strong orientational effects [2,7,8,16,44,45].

As emphasized above, dipolar distortions in a tetrahedral center in an electronic degenerate  $T_1$  or  $T_2$  state only occur if the vibronic coupling with the  $T_2$  modes prevails. However, there may be cases when both the  $E$  and  $T_2$  modes are almost equally active, leading to close values of JTE stabilization energy  $E_{\text{JT}}(E) \approx E_{\text{JT}}(T_2)$  or even  $E_{\text{JT}}(E) > E_{\text{JT}}(T_2)$ . In the latter

case, the JTE distortions are not dipolar. In contrast, in the former case, the APES acquires a two-dimensional trough in mixed  $E$  and  $T_2$  displacements [27], with almost free rotations of the dipolar distortions. Also, in this case, the quadratic terms of vibronic coupling may become significant, leading to the formation of orthorhombic minima of the APES [46].

In a tetrahedral cluster, the JTE-active  $T_2$  type displacements of the dopant and the nearest coordination sphere include three sets of nuclear coordinates. However, as outlined in Sec. II, introducing the so-called Born charge reduces the vibronic coupling to just the displacements of the central atom. In the tunneling model, we describe its dynamics by a single parameter  $\Gamma$ , the reciprocal probability of quantum tunneling through potential barriers between symmetry-equivalent wells on the lower branch of the APES. Including the second and other coordination spheres of the crystals, meaning solving a multimode problem, will not change its one-parameter description: The multimode approach does not change the one-dimensional nature of tunneling [38], and hence, the same model with one tunneling parameter  $\Gamma$  applies.

Note, however, that the tunneling model (and the relevant calculations) assumes low temperatures  $k_B T \lesssim \Gamma$ . On the other hand, JTE active trigonal distortions are observed at much higher temperatures  $k_B T \gg 200 \text{ cm}^{-1}$  [47]. Also, a random strain may lock the system in distorted wells [6,48]. In most of these and other more complicated cases, the model of multiwell APES for the JTE centers remains valid. However, the parameter  $\Gamma$  of the transitions between the minima can be treated as over-the-barrier hopping (instead of tunneling), with the factor  $\exp(-\delta/k_B T)$ , where  $\delta$  is the barrier height between the distorted dipolar configurations. Simultaneously, this activation formula serves as a rather rough model of transitions from one minimum to another. For a more accurate result, it is necessary to temperature-populate the excited tunneling states in the APES minima as well as the excited states of hindered rotations and over-the-barrier reflections in the wrapped potential energy trough, as in the case of spinels with the cooperative JTE [49].

The fundamental cause for the JT-induced symmetry breaking is the gain in adiabatic potential energy due to the improved covalency of the chemical bonds by distortions [2,7,8,30]. Being essentially local, the physical nature of the JTE determines the dopant-site analysis developed in this paper. This approach does not require periodic boundary conditions on the crystal lattice. Successfully applied to ceramics and highly doped semiconductors, an alternative method would consider a supercell with a quasirandom position of several dopants followed by a respective soft-mode analysis [50,51]. For example, in a sphalerite crystal with a 2% dopant concentration, a supercell with four dopant sites per cell would include  $\sim 6400$  atoms, meaning a microcanonical ensemble with four ordered and  $4! = 24$  completely disordered states with shallow disorder wells allowing huge fluctuations.

### B. Parameter values

The tunneling parameter value  $\Gamma$ , as it follows from Eq. (6), is determined by the vibronic coupling constants in the JTE.

An estimate of JTE stabilization energy  $E_{JT}$  can be obtained from the impurity contribution to the crystal elasticity tensor extracted from ultrasound experiments [52]. From the anomalies in the temperature dependence of the ultrasound propagation in ZnSe: Ni<sup>2+</sup> and ZnSe: V<sup>2+</sup> [52,53], the activation barrier between the minima turns out to be  $60 \text{ cm}^{-1}$ . With  $\hbar\omega \approx 120 \text{ cm}^{-1}$ , including the zero-vibration value  $\frac{1}{2}\hbar\omega \approx 60 \text{ cm}^{-1}$ , from Eq. (6) we get for the barrier height  $\frac{1}{4}E_{JT} \approx 120 \text{ cm}^{-1}$ , where from  $E_{JT} \approx 480 \text{ cm}^{-1}$ . The rough estimate gives  $\Gamma \approx 4 \text{ cm}^{-1}$ .

For ZnO: Ni<sup>2+</sup> with the dopant concentration 2%, at room temperature  $k_B T \approx 200 \text{ cm}^{-1}$  and the electric field frequency 50 Hz, the measured value of electric permittivity reaches  $\sim 7130$  [15]. For the pure host crystal ZnO, it is 30. At the above frequency,  $h\nu \ll \Gamma$ , we can assume that the dopant contribution  $7130 - 30 = 7100$  is close to its static value, meaning  $\varepsilon'(0) \approx 7100$ . In our theoretical evaluation, taking as above that  $E_{JT} \approx 480 \text{ cm}^{-1}$ , the orthorhombic saddle points are at  $\frac{1}{4}E_{JT} \approx 120 \text{ cm}^{-1}$  above the APES minima points. With  $\hbar\omega \approx 120 \text{ cm}^{-1}$ , the ground state is  $\frac{1}{2}\hbar\omega \approx 60 \text{ cm}^{-1}$  above the bottom of the wells, and the saddle points of the potential barriers are  $\sim 60 \text{ cm}^{-1}$  above the ground state. Therefore, populated at  $k_B T \approx 200 \text{ cm}^{-1}$ , over-the-barrier excited states contribute significantly to the measured value of  $\varepsilon'$ . Measurements at a lower temperature  $k_B T < 60 \text{ cm}^{-1}$  would yield a lower value of  $\varepsilon'$ , closer to theoretical estimates. In a later publication elsewhere, we will consider the contribution of hindered rotations of the JTE-induced dipolar distortions at higher temperatures.

As it follows from the experimental measurements [15], the further increase of impurity concentration from 2 to 4% lowers the electric permittivity of the system significantly down to  $\varepsilon' \approx 940$  and even less at 5% doping [54]. This dramatic drop in electric permittivity may be due to the dimerization of the impurities at higher concentrations. In the pseudospin-pseudospin “exchange” coupling, negative values of the exchange parameter result in a ground-state vibronic singlet [55] with zero polarizability  $\chi = 0$ . Lowering the local symmetry removes the electronic degeneracy and quenches the JTE-induced dipolar distortions.

## VIII. CONCLUSIONS

Solid-state orientational polarizability, meaning the presence of free (or hindered)-rotating ready-made dipolar groups in solids like in polar liquids and gases, assumed to be possible by Debye [1] more than a century ago, was shown in our works to follow directly from the JTE (in noncentrosymmetric polyatomic systems) and PJTE (in both centrosymmetric and noncentrosymmetric systems) that induce local dipolar distortions, rigorously described in this paper. A characteristic of the JTE is that the APES at the high-symmetry point is shaped like a sharp-vertex cone. In the case of a PJTE, it is a round-head maximum. In both cases, around the high-symmetry point, the sombrero-like lower branch of the APES has a wrapped trough with an off-center broken symmetry at its bottom. The off-center instability benefits covalency; the off-center distortion improves the covalent chemical bonding in the JTE site. In both cases, the tetrahedral sites with the JTE for a  $T$  term or the cubic site with the PJTE, the landscape of the trough is

as shown in Fig. 3. Approximately, its angular dependence has the extended cubic-field Devonshire-O'Brien form of Eq. (4).

In most solids with the JTE or PJTE, the high-symmetry central maximum is relatively high, with the JTE stabilization energy  $E_{JT} > k_B T$ . Therefore, the vibronic states penetrating directly through or over the central maximum are not thermally populated at room temperature. The off-center atomic motion follows the trough around the high-symmetry point of the APES. With no electric field applied, it remains evenly spread over the equivalent minima of the trough, yet the instantaneous value of the dipole moment of a given dopant may be about its maximum magnitude  $p_0$  in the wells at the bottom of the trough. Due to the symmetry equivalence of the minima, the zero-field average polarization per site is zero.

Under a nonzero electric field, the off-center trough is slant. The nuclear motion localizes at its lowest minimum

by moving along the trough around the conic vertex of the APES or its round-head maximum. In other words, the electric field applies a torque on the local dipole, turning it into alignment along the trough around the high-symmetry point. This effect is like the orientational polarization of polar liquids, as predicted by Debye [1]. The JTE-induced nonzero value of the dipole moment is proportional to the trough radius  $p_0 \propto R_0$ . With temperature approaching zero, the polarization has a jump discontinuity from zero at  $E = 0$  to a nonzero value at any small  $E \neq 0$ . Therefore, the transition to the nonzero dipole moment is sudden in a dopant site with the JTE for the ground-state  $T$  term. In such a case, the corresponding value of the orientational susceptibility approaches infinity at low temperatures. In a cubic site with the PJTE with a nondegenerate ground state, this transition is smooth throughout the applied electric field of the order of  $E_{cr} \propto \sqrt{(\Gamma k_B T)/p_0}$ .

- 
- [1] P. J. W. Debye, Einige Resultate einer kinetischen Theorie der Isolatoren, *Phys. Z.* **13**, 97 (1912) [in *The Collected Papers of Peter J. W. Debye* (Ox Bow Press, Woodbridge, CT, 1988), pp. 173–179]; *Polar Molecules* (Literary Licensing, LLC, Whitefish, 2012), Sec. 7, pp. 27–30.
- [2] I. B. Bersuker, On the origin of ferroelectricity in perovskite-type crystals, *Phys. Lett.* **20**, 589 (1966).
- [3] E. Teller, Foreword: An historical note, in *The Jahn-Teller Effect in Molecules and Crystals*, by R. Englman, (Wiley-Interscience, London, 1972); The Jahn-Teller effect—Its history and applicability, *Physica A* **114**, 14 (1982).
- [4] H. A. Jahn and E. Teller, Stability of polyatomic molecules in degenerate electronic states. I—Orbital degeneracy, *Proc. R. Soc. Lond. A* **161**, 220 (1937).
- [5] R. Englman, *The Jahn-Teller Effect in Molecules and Crystals* (Wiley-Interscience, London, 1972).
- [6] F. S. Ham, Jahn–Teller effects in electron paramagnetic resonance spectra, in *Electron Paramagnetic Resonance*, edited by S. Geschwind (Plenum, New York, 1972), pp. 1–119.
- [7] I. B. Bersuker and V. Z. Polinger, *Vibronic Interactions in Molecules and Crystals*, Springer Series in Chemical Physics (Springer-Verlag, Berlin, 1989), Vol. 49.
- [8] I. B. Bersuker, *The Jahn-Teller Effect* (Cambridge University Press, Cambridge, 2006).
- [9] I. B. Bersuker, Four modifications of the Jahn-Teller effect. The problem of observables: Spin-orbital interaction, tunneling splitting, orientational polarization, *Phys. Chem. Chem. Phys.* **25**, 1556 (2023).
- [10] A. Ceulemans, *The Theory of the Jahn-Teller Effect: When a Boson Meets a Fermion* (Springer, Cham, 2022).
- [11] J. H. Van Vleck, The Jahn-Teller effect and crystalline stark splitting for clusters of the form  $XY_6$ , *J. Chem. Phys.* **7**, 72 (1939).
- [12] U. Öpik and M. H. L. Pryce, Studies of the Jahn-Teller effect. I. A survey of the static problem, *Proc. R. Soc. Lond. A* **238**, 425 (1957).
- [13] S. F. Dubinin, V. I. Sokolov, V. D. Parkhomenko, V. I. Maksimov, and N. B. Gruzdev, Effect of doping with nickel ions on the structural state of a zinc oxide crystal, *Phys. Solid State* **51**, 2019 (2009).
- [14] E. V. Lavrov, F. Herklotz, and Y. S. Kutin, Effect of uniaxial stress on substitutional Ni in ZnO, *Solid State Commun.* **159**, 36 (2013).
- [15] M. Ashokkumar and S. Muthukumar, Effect of Ni doping on electrical, photoluminescence and magnetic behavior of Cu doped ZnO nanoparticles, *J. Lumin.* **162**, 97 (2015).
- [16] I. B. Bersuker, Vibronic (pseudo Jahn-Teller) theory of ferroelectricity: novel aspects and applications, *Ferroelectrics* **536**, 1 (2018).
- [17] I. B. Bersuker and V. Z. Polinger, Perovskite crystals: unique pseudo-Jahn-Teller origin of ferroelectricity, multiferroicity, permittivity, flexoelectricity, and polar nanoregions, *Condens. Matter* **5**, 68 (2020).
- [18] Here and below, matrices are denoted by Roman bold type. Three-vectors have an arrow above the respective character,  $\vec{A}$ , or are represented like  $(A_x, A_y, A_z)$ , if written in components.
- [19] M. Born and K. Huang, *Dynamical Theory of Crystal Lattices* (Oxford Academic, New York, 1996); J. D. Axe, Apparent ionic charges and vibrational eigenmodes of BaTiO<sub>3</sub> and other perovskites, *Phys. Rev.* **157**, 429 (1967).
- [20] I. B. Bersuker, *Electronic Structure and Properties of Transition Metal Compounds* (Wiley, Hoboken, 2010), Sec. 8.2, p. 411.
- [21] In some cases, even in a strong crystal field, the electron configuration is dominated by a strong electron repulsion, lowering the energy of the high-spin configuration and creating the ground-state term.
- [22] A. D. Lier, Topological aspects of the conformational stability problem. Part I. Degenerate electronic states, *J. Phys. Chem.* **67**, 389 (1963).
- [23] R. S. Dagis and I. B. Levinson, Group-theoretical properties of the adiabatic potential in molecules, in *Optika i Spektroskopija. Sbornik Statei. III. Molekuljarnaja Spektroskopija*, edited by S. E. Frish (Nauka, Leningrad, 1967), p. 3.
- [24] P. Pelikán and M. Breza, Group-theoretical analysis of the possible symmetries of the Jahn-Teller systems, *J. Mol. Struct. THEOCHEM* **124**, 231 (1985).
- [25] A. Ceulemans, The structure of Jahn-Teller surfaces, *J. Chem. Phys.* **87**, 5374 (1987).
- [26] A. F. Devonshire, The rotation of molecules in fields of octahedral symmetry, *Proc. R. Soc. Lond. A* **153**, 601 (1936).

- [27] H. U. Beyeler, The hindered rotation in various fields of cubic symmetry, *Phys. Status Solidi B* **52**, 419 (1972).
- [28] M. C. M. O'Brien, Dynamic Jahn-Teller effect in an orbital triplet state coupled to both  $E_g$  and  $T_{2g}$  vibrations, *Phys. Rev.* **187**, 407 (1969).
- [29] I. B. Bersuker, Pseudo Jahn-Teller origin of perovskite multi-ferroics, magnetic-ferroelectric crossover, and magnetoelectric effects: The  $d^0 - d^{10}$  problem, *Phys. Rev. Lett.* **108**, 137202 (2012).
- [30] I. B. Bersuker, N. N. Gorinchoi, and V. Z. Polinger, On the origin of dynamic instability of molecular systems, *Theor. Chim. Acta* **66**, 161 (1984); MO LCAO analysis of the vibronic instability of the  $\text{CuCl}_5^{2-}$  trigonal bipyramidal configuration. Critical view on the angular overlap model in vibronic problems, *Chem. Phys.* **159**, 75 (1992); Pseudo Jahn-Teller origin of square-planar configuration instability of main-group-element hydrides, *J. Mol. Struct.* **270**, 369 (1992).
- [31] M. C. M. O'Brien, The Berry phase in a  $T(X) \tau_2$  Jahn-Teller system, with a note on tunneling, *J. Phys. A* **22**, 1779 (1989).
- [32] F. S. Ham, The role of Berry's phase in ordering the low-energy states of a  $T \times \tau_2$  Jahn-Teller system in strong coupling, *J. Phys.: Condens. Matter* **2**, 1163 (1990).
- [33] H. Koizumi, I. B. Bersuker, J. E. Boggs, and V. Z. Polinger, Multiple lines of conical intersections and nondegenerate ground state in  $T \otimes t_2$  Jahn-Teller systems, *J. Chem. Phys.* **112**, 8470 (2000).
- [34] A. Bohm, A. Mostafazadeh, H. Koizumi, Q. Niu, and J. Zwanziger, A brief review of point groups of molecules with applications to Jahn-Teller systems, in *The Geometric Phase in Quantum Systems* (Springer, Berlin, 2003), pp. 407–427.
- [35] M. Gomez, S. P. Bowen, and J. A. Krumhansl, Physical properties of an off-center impurity in the tunneling approximation, I. Statics, *Phys. Rev.* **153**, 1009 (1967).
- [36] F. Bridges, Paraelectric phenomena, *CRC Crit. Rev. Solid State Mater. Sci.* **5**, 1 (1975).
- [37] I. B. Bersuker, Inversion splitting of energy levels in free transition metal complexes, *Zh. Eksp. Teor. Fiz.* **43**, 1315 (1962) [*JETP* **16**, 933 (1963)].
- [38] V. Z. Polinger, Tunnel splitting in tetragonal and trigonal distorted Jahn-Teller systems, *Fiz. Tverd. Tela* **16**, 2578 (1974) [*Sov. Phys. Solid State* **16**, 1676 (1975)]; Tunneling in Jahn-Teller Systems and multidimensional WKB approximation, *Adv. Quantum Chem.* **44**, 59 (2003); V. Z. Polinger, C. A. Bates, and J. L. Dunn, Tunneling splitting and relaxation in the multimode  $T \otimes t_2$  Jahn-Teller system, *J. Phys.: Condens. Matter* **10**, 1293 (1998).
- [39] M. D. Sturge, The Jahn-Teller effect in solids, *Solid State Phys.* **20**, 91 (1968).
- [40] M. C. M. O'Brien, Reduction factors, tunneling splitting and zero-phonon line intensity in  $T \otimes \tau_2$  and  $T \otimes (\tau_2 \otimes \epsilon)$  Jahn-Teller systems, *J. Phys.: Condens. Matter* **2**, 5539 (1990).
- [41] M. C. M. O'Brien, The dynamic Jahn-Teller effect with many frequencies: A simple approach to a complicated problem, *J. Phys. C* **5**, 2045 (1972).
- [42] V. Polinger and I. B. Bersuker, Pseudo Jahn-Teller effect in permittivity of ferroelectric perovskites, *J. Phys. Conf. Ser.* **833**, 012012 (2017).
- [43] J. H. Van Vleck, Chapter II, Classical theory of the Langevin-Debye formula, in *The Theory of Electric and Magnetic Susceptibilities* (Clarendon Press, Oxford, 1932).
- [44] I. B. Bersuker, Pseudo Jahn-Teller effect in the origin of enhanced flexoelectricity, *Appl. Phys. Lett.* **106**, 022903 (2015); Giant permittivity and electrostriction induced by dynamic Jahn-Teller and pseudo Jahn-Teller effects, **107**, 202904 (2015).
- [45] V. Polinger, Off-center instability of  $\text{Nb}_{5+}$  in  $\text{KNbO}_3$  under ambient pressure, *Chem. Phys.* **459**, 72 (2015); G. I. Bersuker, and V. Z. Polinger, Multimode pseudo Jahn-teller effect for off-centre impurities in crystals, *Phys. Status Solidi B* **125**, 401 (1984).
- [46] I. B. Bersuker and V. Z. Polinger, Jahn-Teller effect for  $T$  terms, *Zh. Eksp. Teor. Fiz.* **66**, 2078 (1974) [*JETP* **39**, 1023 (1974)].
- [47] B. Ravel, E. A. Stern, R. I. Vedral, and V. Kraizman, Local structure and the phase transitions of  $\text{BaTiO}_3$ , *Ferroelectrics* **206**, 407 (1998).
- [48] F. S. Ham, Dynamical Jahn-Teller effect in paramagnetic resonance spectra: Orbital reduction factors and partial quenching of spin-orbit interaction, *Phys. Rev.* **138**, A1727 (1965).
- [49] R. Englman and B. Halperin, Cooperative dynamic Jahn-Teller effect. I. Molecular field treatment of spinels, *Phys. Rev. B* **2**, 75 (1970).
- [50] L. G. Wang and A. Zunger, Phosphorus and sulfur doping of diamond, *Phys. Rev. B* **66**, 161202(R) (2002).
- [51] D. S. Sholl and J. A. Steckel, *Density Functional Theory: A Practical Introduction Second Edition* (Wiley, Hoboken, 2023), Chap. 2, p. 29.
- [52] V. V. Gudkov and I. B. Bersuker, Experimental evaluation of Jahn-Teller effect parameters by means of ultrasonic measurements. application to impurity centers in crystals, in *Vibronic Interactions and the Jahn-Teller Effect. Progress in Theoretical Chemistry and Physics*, edited by M. Atanasov, C. Daul, and P. L. W. Tregenna-Piggott (Springer, Dordrecht, 2012), Vol. 23, Chap. 7, p. 143.
- [53] N. S. Averkiev, I. B. Bersuker, V. V. Gudkov, I. V. Zhevstovskikh, M. N. Sarychev, S. Zherlitsyn, S. Yasin, G. S. Shakurov, V. A. Ulanov, and V. T. Surikov, The Jahn-Teller effect in elastic moduli of cubic crystals: General theory and application to strontium fluorite doped with chromium ions, in *Fluorite: Structure, Chemistry and Applications*, edited by M. van Asten (Nova Science, New York, 2019), Chap. 2, p. 111.
- [54] P. Norouzzadeh, Kh. Mabhouti, M. M. Golzan, and R. Naderali, Comparative study on dielectric and structural properties of undoped, Mn-doped, and Ni-doped  $\text{ZnO}$  nanoparticles by impedance spectroscopy analysis, *J. Mater. Sci. – Mater. Electron.* **31**, 7335 (2020).
- [55] D. I. Khomskii and S. V. Streltsov, Orbital effects in solids: Basics, recent progress, and opportunities, *Chem. Rev.* **121**, 2992 (2021).